2019•2020

Faculteit Industriële ingenieurswetenschappen

master in de industriële wetenschappen: elektromechanica

Masterthesis

Investigation of process disturbances in femtosecond laser texturing of stainless steel

PROMOTOR :

Prof. dr. ir. Albert VAN BAEL

PROMOTOR :

Prof. Stefan DIMOV

prof. Richard HALL

BEGELEIDER :

ing. Tim EVENS

COPROMOTOR :

Prof. dr. ir. Sylvie CASTAGNE

BEGELEIDER :

MSc. Aleksandra MICHALEK

dr. Balasubramanian NAGARAJAN

Dieter Baeten

Scriptie ingediend tot het behalen van de graad van master in de industriële wetenschappen: elektromechanica

Gezamenlijke opleiding UHasselt en KU Leuven

2019 • 2020

Faculteit Industriële ingenieurswetenschappen

master in de industriële wetenschappen: elektromechanica

Masterthesis

Investigation of process disturbances in femtosecond laser texturing of stainless steel

PROMOTOR :

Prof. dr. ir. Albert VAN BAEL

PROMOTOR :

Prof. Stefan DIMOV

prof. Richard HALL

BEGELEIDER :

ing. Tim EVENS

COPROMOTOR :

Prof. dr. ir. Sylvie CASTAGNE

BEGELEIDER :

MSc. Aleksandra MICHALEK

dr. Balasubramanian NAGARAJAN

Dieter Baeten

Scriptie ingediend tot het behalen van de graad van master in de industriële wetenschappen: elektromechanica

UHASSELT KU LEUVEN

Deze masterproef werd geschreven tijdens de COVID-19 crisis in 2020. Deze wereldwijde gezondheidscrisis heeft mogelijk een impact gehad op de opdracht, de onderzoekshandelingen en de onderzoeksresultaten.

Preface

This thesis describes the research I realized at the School of Engineering in Birmingham. This was possible because of the collaboration between the Manufacturing group of Prof. Dimov in Birmingham and Cel Kunststoffen with Prof. Van Bael in Diepenbeek. My time at the school of Engineering was very educational and interesting, both on a technical and personal level.

First and foremost, I would like to thank the people who helped to realise this thesis. This includes my promoter in Belgium, Prof. Albert Van Bael and my promoter in Birmingham, Prof. Stefan Dimov. Their support and guidance helped me to create this work. Next, I would like to thank Prof. Sylvie Castagne, Prof. Richard Hall and Ing. Tim Evens, who also provided guidance throughout the process of the thesis. Furthermore, I want to thank my daily promoter in Birmingham, Aleksandra Michalek for all the help and advice regarding laser processing and Balasubramanian Nagarajan in Belgium, who provided guidance for the modelling of this thesis. Also, I would like to thank both universities, the School of Engineering and KU Leuven to make this exchange possible.

Finally, I want to mention some other people. First of all, my parents, for their support and the confidence they have in me. Also, my housemates in Birmingham who made me really feel at home in my new environment and supported me every day. And most importantly, my partner, whose motivational words and support made it possible to finish this work in these desperate times of Covid-19.

Table of contents

List of tables

List of figures

Abstract

The Manufacturing research group from the school of Engineering in Birmingham examines the possibilities and applications for laser processing. This master's thesis researches the two main disturbances for laser processing: the Focal Offset Distance (FOD) and the Beam Incident Angle (BIA). These factors are not yet examined for femtosecond lasering, but their effects are needed for laser manufacturers and users. Furthermore, this master's thesis also evaluates a theoretical femtosecond ablation model and makes suggestions to improve and expand upon this model to include the above-mentioned disturbances.

These influences are examined on AISI 316 samples, by lasering a matrix with different processing parameters and repeating this for different disturbance values. The influence on texture lasering of these disturbances is determined based on scans made of these lasered samples. The ablation model is used to compare theoretical with the experimental results.

The experiments show large influences on the groove depth caused by these disturbances. The FOD gradually decreases the depth of the grooves, whereas the BIA is affected by the smallest tested angle. These influences can be used by manufacturers of lasers to partition 3D/free-form surfaces, i.e. to create optimal operating margins for surfaces and materials, so they can determine optimal processing speeds for the industrial applications. The model values deviated slightly from the experiments and some improvements were given, e.g. ways to implement the disturbances.

Abstract in Dutch

De Manufactoring research group of the school of Engineering in Birmingham onderzoekt de mogelijkheden van laser processing en beïnvloedende factoren. Deze masterproef onderzoekt de twee hoofd verstoringen: de Focal Offset Distance (FOD) en de Beam Incident Angle (BIA). Deze factoren zijn nog niet onderzocht voor femtosecond lasering maar de effecten ervan zijn wel nodig voor laser producenten en gebruikers. Verder evalueert deze masterproef ook een theoretisch model voor femtoseconde laser ablatie en geeft suggesties om dit model te verbeteren en uit te breiden om deze verstoringen mee te verwerken.

De verstoringen zijn onderzocht op AISI 316 monsters, door een matrix van proces parameters erop te laseren en dit te herhalen voor verschillende stoorwaarden. De invloed van deze verstoringen wordt vastgesteld gebaseerd op scans van de monsters. Het model wordt gebruikt om theoretische en experimentele waarden te vergelijken.

De experimenten tonen grote invloeden op de groefdiepte door de verstoringen. De FOD verlaagt de groefdiepte geleidelijk terwijl de BIA een direct effect heeft. Deze invloeden kunnen gebruikt worden door producenten van lasers om optimale procesmarges van materialen en oppervlakken te definiëren, zodat optimale productiesnelheden opgesteld kunnen worden voor industriële toepassingen. Het model gaf licht afwijkende waarden in vergelijking met de experimenten. Verder zijn enkele verbeteringen en mogelijkheden om het model te verbeteren gegeven, zoals het verwerken van deze verstoringen.

1 Introduction

1.1 Scope

This master's thesis is carried out at the Laser processing group headed by Prof. Dimov of the Advanced Manufacturing Technology Centre of the University of Birmingham. The thesis is part of the collaboration of Prof. Dimov with Prof. Van Bael of *Cel Kunststoffen*, i.e. the research group on polymer processing of KU Leuven at Campus Diepenbeek, Prof. Castagne of the Manufacturing Processes and Systems Division at the Department of Mechanical Engineering of KU Leuven, and Prof. Hall from the University of Sheffield, who is bringing in industrial considerations and needs particularly from the nuclear sector for surfaces in aggressive environments.

The Advanced Manufacturing Technology Centre builds upon manufacturing engineering and conducts research centred around Advanced Machining, Automation and Intelligent Manufacturing, Laser Processing, Micro Manufacturing and Computer Aided Engineering [1]. The Laser Processing group focuses on research on surface structuring, texturing and polishing of 3D components, in a wide range of materials [2]. The group has two lasers for micromachining, the one with 5 mechanical axes and 2 optical axes was used for this research, as can be seen in Figure 1. The laser can process with a nano- and femtosecond source. Figure 1 also shows the high-resolution characterisation equipment Alicona G5.

There is an increasing demand from the industry for functionalised surfaces [3]. These surface textures can be applied using a different number of techniques. One possibility is nano- or femtosecond laser processing. Some of these functions include hydrophobicity, self-cleaning, corrosion resistance, antimicrobial, antireflection, light transmission enhancement, anti-icing and friction reduction [4],[5]. Specifically for the polymer industry, applying these functional surface textures to products is very interesting, e.g. antibacterial properties for micro injection moulded implants used in medical applications or hydrophobic functionalities for cell phone covers [6]. This can be done by fabricating the replica of the desired structure in the injection mould using laser processing. This way, products with a functional surface can be produced at a high speed and with low processing cost, as is desired for the polymer industry [7]. If the functionality is not directly applied during the forming process, it needs to be applied after the moulding step, resulting in long post-processing times that would not make economic sense [8]. In the nuclear sector, there is demand for these functional surfaces as well. In many reactors, molten salts are present that form a highly corrosive environment. Functional surfaces could increase the corrosion and wear resistance, so the used materials will degrade at a slower rate. Very few tests have been done so far. Initial research shows that lasering reduces the corrosion resistance, however it is also mentioned that the corrosion resistance is largely dependent on the micro structure and surface finish of the sample [9],[10]. So this could possibly result in a net increase of corrosion resistance. Shin et al. [11] highlighted that the outlet temperature of the coolant of such a reactor is kept below 450°C, only to keep the corrosion rate of the materials low enough to reach the design lifetime, to illustrate the importance of the resistance.

As of this date, there is very little research being conducted on freeform or complex surfaces. Most of the research works still focus on flat surfaces but is not sufficient to texturize the complex injection moulds or reactor parts.

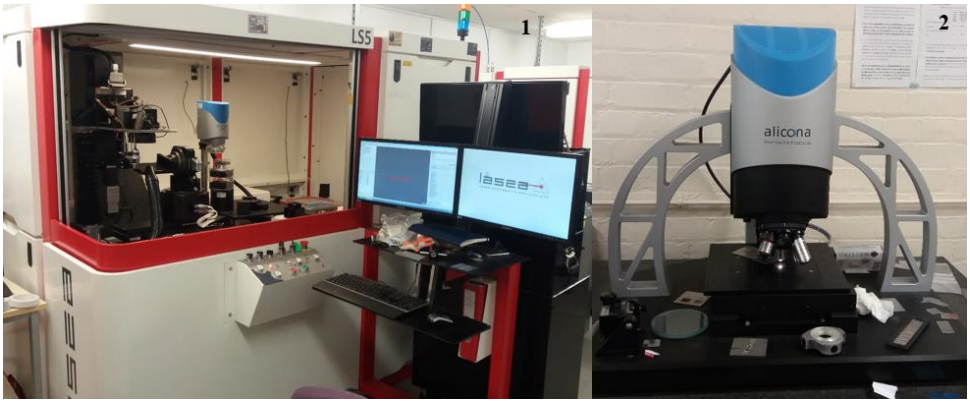

Figure 1: The laser processor (1 and the Alicona IF G5 microscope system (2).

1.2 Problem Definition

Because of the limited research on freeform surfaces, it remains unclear which textures can be lasered onto these surfaces. Most studies are executed on flat surfaces exclusively or focus mainly on the laser parameters that will have an influence when processing a complex surface. For example, there has been a research that examines the geometrical distortion created when lasering and projecting a 2D image on a 3D surface with a nanosecond laser [12]. This was however on a macro level, like how a circle becomes elliptical in shape while not projected perpendicular to the surface. To examine these freeform surfaces, disturbances that would occur when lasering complex shapes need to be examined.

Two of the main disturbances are the Beam Incident Angle (BIA) and Focal Offset Distance (FOD), but their effect on complex surfaces has not been thoroughly studied. The BIA is the angle between the laser beam and the normal of the surface as Figure 2 illustrates. Figure 2 also shows that the FOD is the distance between the focus point of the laser, and the actual surface of the workpiece. Limitations and the influence of the BIA and FOD have been examined by Garcia et al. [4] for a nanosecond laser to correlate changes in a defined pattern. But femtosecond lasering is very different from nanosecond lasering because there is no thermal influence [13], so this needs to be verified for femtosecond lasering. Previous research within the laser processing research group has shown the basic parameters to create a lotus leaf inspired structure and Laser Induced Periodic Surface Structures (LIPSS) on a flat surface for different materials [14]. The LIPSS are nano-structures and also have functional properties, like wetting, friction or optical [15].

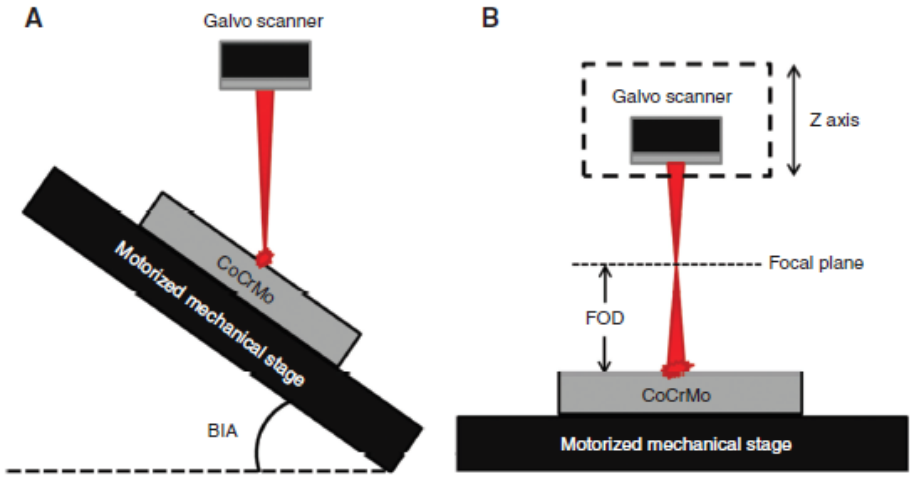

Figure 2: Schematic diagram of BIA and FOD [13, p.4].

To the best of my knowledge, there has yet to be a study that examines the main disturbances BIA and FOD for femtosecond laser texturing. This is needed to form a bridge between flat surface research and the requested complex surfaces for the industry. Another research, somewhat related to the BIA, explains that a relation between the BIA and the ablation threshold, i.e. the minimum required energy to ablate the material, exists [16]. It is shown that different polarisation of laser beams influences the threshold when the incident angle increases, caused by Fresnel reflection.

In addition to this, the existing models of femtosecond laser ablation are still in their early stages. The models only calculate the ablation depth in a very basic manner, i.e. making a lot of assumptions and simplifications. These models do not include the influence of disturbances yet.

1.3 Objectives

The main objective of this research is to analyse the disturbances that occur in a flat surface setting to form a basis for further research on these influences for lasering on complex shapes. The tested material is a corrosion resistant tool steel (AISI 316) and is commonly used for injection moulds and for nuclear applications. These common corrosion resistant steels are very frequently used in reactors. Additional research will be carried out to find an acceptable range for the disturbances for this material, i.e. resulting laser grooves that have still a desired depth and FWHM.

The influence of the disturbances is important to analyse because this can then be used for industrial applications, especially laser texturing of 3D components and tooling inserts. When these influences are known, they can be used for pre-calculating and pre-processing of the CAD data for samples. To do this, the surfaces and materials should be partitioned, i.e. tolerances for each material should be made. With this knowledge, it is possible to increase the overall processing speed when using lasers to process 3D surfaces [17]. The influences are also needed to examine the possibilities of using basic laser processors for texturing complex shapes, because these lasers have less manoeuvrability than the more advances lasers.

Furthermore, the gathered data will be used to compare values given by a current femtosecond ablation model, based on [18], [19]. The created model has so far only been briefly verified to achieve similar results as these described in the papers. In other words, it has not been used to verify experiments. The model

predicts the depth and general shape of a groove or hole with a set of laser parameters. The model can be used to reduce the amount of experiments done, e.g. with the model results, only some verification experiments need to be conducted, instead of a full examination, because this is done with the model. The model can also be used for pre-calculating laser executions for the industry, i.e. to calculate the laser settings when a certain depth is desired. Finally, suggestions are given of how to adjust the model to include the disturbances and possibly other effects. Including these disturbances in the model can prove useful to also allow the model to be used for the CAD pre-calculating and pre-processing

As for the application for the polymer industry, the actual replication process will be performed by Cel Kunststoffen in a further study. Textured injection moulds will be used, and the replicated parts will be studied to see how well the texture and wetting properties are transferred to the parts, and if there are defects because of demoulding.

1.4 Method

Firstly, the influence of disturbances during the laser texturing of corrosion stool steel will be investigated by experiments. In order to achieve process optimization, a range of scanning speed and number of layers are tested. These fixed combinations of the laser parameters will then be repeated for different disturbance values. To perform these experiments, the samples need to be properly prepared.

To start the preparation, the samples will be cut to the desired dimensions. The maximum laser surface is 60x60 mm. Next, the samples can be texturized with the laser. A simple geometry will be used, i.e. a set of parallel lines. Grooved patterns were obtained for different combinations of scanning speed and number of layers. This will then be repeated for different values of BIA and FOD.
Then, the structures will be examined with the Alicona G5 to visualise and investigate the resulting grooves. Also, different parameters such as the depth of the groove and the Full Width at Half Maximum (FWHM) will be measured.
With this large dataset, the laser ablation model will be checked and compared to the experimental results. Some suggestions to implement the disturbances will be made, next to some other general improvements for the model.

2 Literature study

The discussed topics of this study start with basic laser properties, including pulse duration, wavelength, pulse energy, beam spot size and laser fluence. Also, the ablation threshold of the material is discussed. Then characterisation methods and parameters are discussed. This includes focus variation, a method used to make a 3D image of the structure. This is followed by a contact angle explanation, because it is a commonly used parameter for discussing wettability, which is explained after, including the Wenzel and Cassie-Baxter wetting models. Then a small part is dedicated for the explanation of demoulding of polymers with micro features, as a possible and interesting application. First the replication of the features is discussed, followed by both 2D and 3D examples. For another application, the corrosion resistance is explained for the nuclear sector and why this is an important factor. Some corrosion tests specifically done on stainless steel are discussed here as well.

2.1 (Basic) Laser properties

2.1.1 Pulse duration

Within laser processing, there is a wide range of applications. These include laser cutting, drilling and ablation [20]. A major difference between laser setups is the duration of a single pulse, when using a pulsed energy distribution. The pulse duration ranges from microseconds, used in most laser cutting applications, to femto seconds (=$10^{-15}s$), mostly used for ablation, i.e. the direct evaporation of materials.

The main difference between nano- and femtosecond laser processing is that the process is mainly thermal with nanosecond laser irradiation or long pulses, i.e. pulse durations longer than 100ps. This means that the material is actually melted, and as a result, forms a recast layer and has a large heat affected zone (HAZ). This can change the microstructure of the material due to possible recrystallization initiated by the high temperatures. For femtosecond laser processing or ultra-short pulse, i.e. pulse duration shorter than 10ps, the process is mainly photonic in nature. This means that the material is instantly vaporized which results in the absence of a HAZ or recast layer. This is because the pulses are short enough that the added heat mainly goes to the evaporated material, and the rest heat fraction can spread to the rest of the material. Only in extreme cases, with low speeds and many repetitions, there is a possibility of heat build-up [21]. Figure 3 shows lines lasered with a femtosecond (a-c) and a nanosecond laser (d-f). This shows that nanosecond lasering has rougher edges, because the material is melted and sometimes sputtered around the lasered area. The femtosecond laser however has smoother edges because of the direct evaporation of the material.

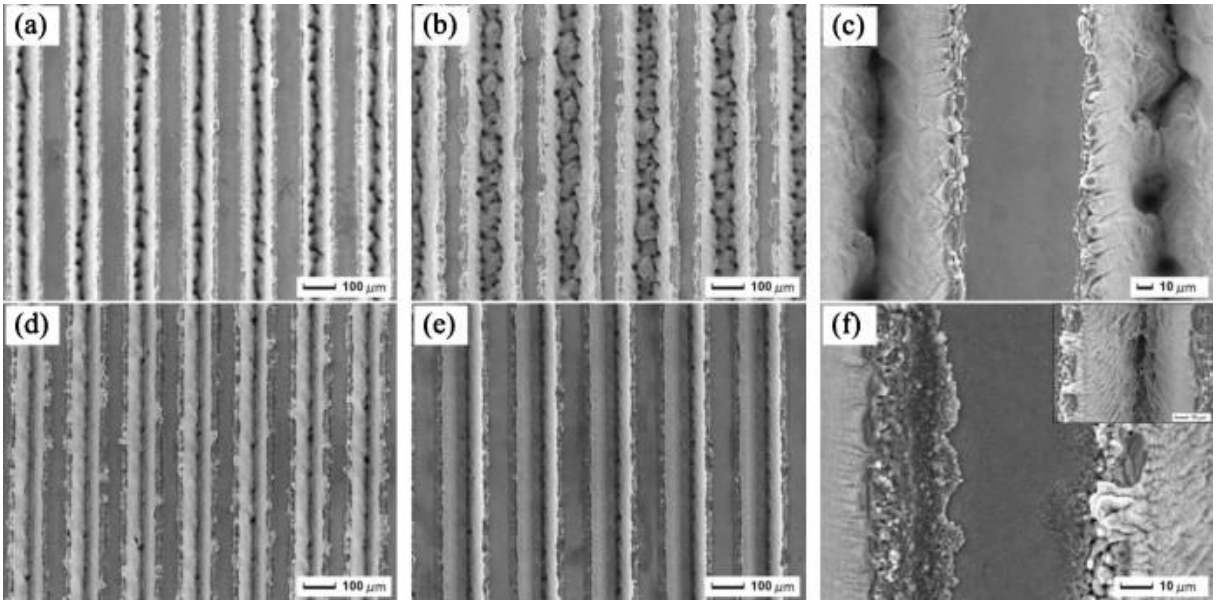

Figure 3: Femtosecond lasering example (a, b and c) and nanosecond lasering (d, e and f) [22, p.46].

2.1.2 Wavelength

The used wavelength is an important parameter of the laser source. The wavelength is the distance between two of the same points of a wave, e.g. the tops of a sine wave [23]. The most common range for femtosecond laser sources ranges between 720-1060 nm [24],[25]. This range falls within the Infrared (IR) spectrum and as such, is not part of the visible spectrum (380-740 nm), as illustrated in Figure 4. For many non-metals and even some metals like copper, shorter wavelengths are used [26].

It is important to know the wavelength of the laser because the wavelength relates to the energy of the light. The longer the wavelength, the lower the frequency which results in a lower energy, according to Planck's equation [27] [20].

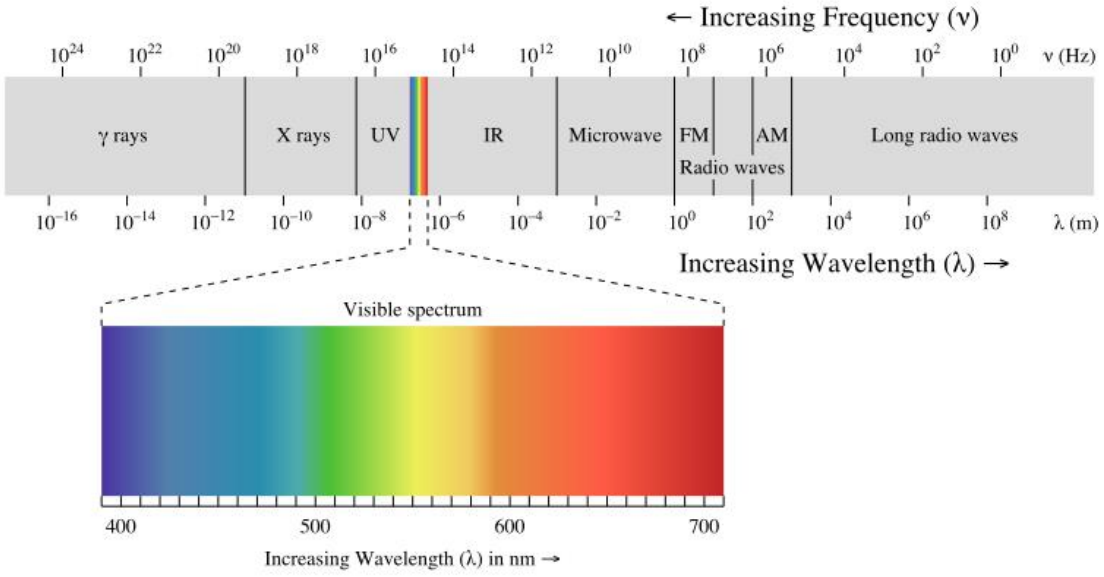

Figure 4: The electromagnetic spectrum [27].

2.1.3 Pulse energy, fluence and beam spot size

The pulse energy (E) in a pulsed energy distribution can be calculated by dividing the average power of the laser (P) by the pulse repetition rate (f_r) i.e. the frequency of the pulses or number of pulses per second. These parameters can be adjusted in the laser system.

The fluence (ϕ) of a laser beam is a value that is commonly used when discussing laser processing. The fluence is the energy density of the beam at the beam spot on the surface, i.e. the energy delivered in a specified area. It can be calculated using Eq. (1) and is typically expressed in J/cm² [21]. The laser fluence however is not an adjustable parameter. It needs to be calculated from the pulse energy and the beam spot size. The peak fluence is a very similar parameter as the fluence. It is defined as the double of the normal fluence for a Gaussian beam [19].

$$\phi = \frac{P}{f_p \cdot A} \tag{1}$$

When describing the laser beam shape, it is commonly referred to as a Gaussian beam, illustrated in Figure 5. A related laser parameter is the M² value, or the common measure of beam propagation. It is a value to describe how good the beam follows a Gaussian distribution, and thus, how close the beam follows the Gaussian simplification. A value of M² lower than 1.3 is generally considered to be a good beam quality [21],[28]. Figure 5 also shows the change in the beam radius in accordance with the out of focus depth, z. Here it can be seen that the beam diameter has a minimum value at z = 0. This is called the focus or the beam waist. Because this is the smallest spot of the laser beam, the highest fluence can be achieved here. The further you are from the focus, the lower the fluence will be. A common term in laser processing is the Rayleigh length. This is the distance from the focus where the area of the beam spot is doubled, or the beam radius is $\sqrt{2}$ times larger than in the focus. This is illustrated with z_r in Figure 5. It can also be seen that the laser beam has a profile comparable to a cosines hyperbolic function when looking at the cross section. It can also be compared to a cooling tower of a power plant or a diablo toy.

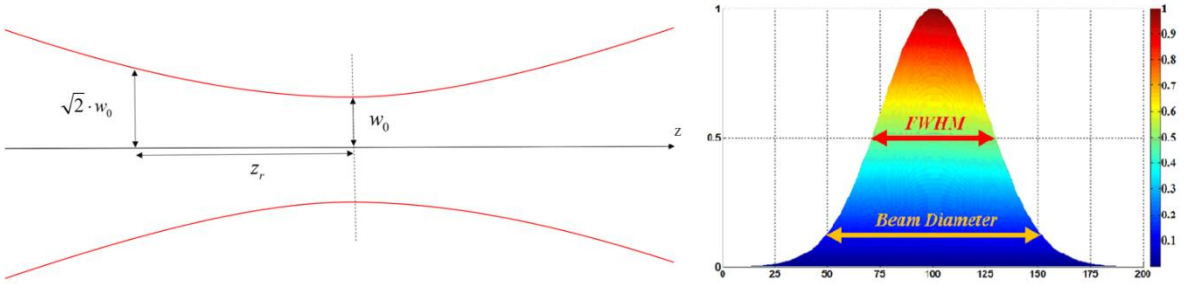

Figure 5: Beam radius related to z (left) and the Gaussian beam shape (right) [29].

2.1.4 Ablation threshold

The ablation threshold is the lowest amount of needed energy to ablate the material. This is a material parameter and is theoretically always the same. There is however a phenomenon where the threshold changes when laser processing. It was shown that when multiple laser pulses are shot at the same spot, the ablation threshold lowers [30], [31]. This leads to the possibility of being able to laser with fluences lower than the ablation threshold for repeated pulses.

Other than this, the ablation threshold can be influenced by the thickness of the sample, as shown in [30]. This is however only the case for very thin samples or films. Tungsten on silicon substrate was used here, with picosecond lasering, and the limit where the threshold changed was determined to be 95 nm. Thicker samples showed the same ablation threshold.

2.2 Measurements and characterization techniques

2.2.1 Focus variation

Focus variation is a technique to combine the small depth of focus of an optical system with vertical scanning [32]. With the use of a beam splitting mirror, light is focused on the sample. A light sensor detects all the reflected light from the sample as is illustrated in Figure 6. This sensor data, which is a 2D image, can then be saved and later combined with other scans to reconstruct a 3D image. This results in topographical and colour information [33].

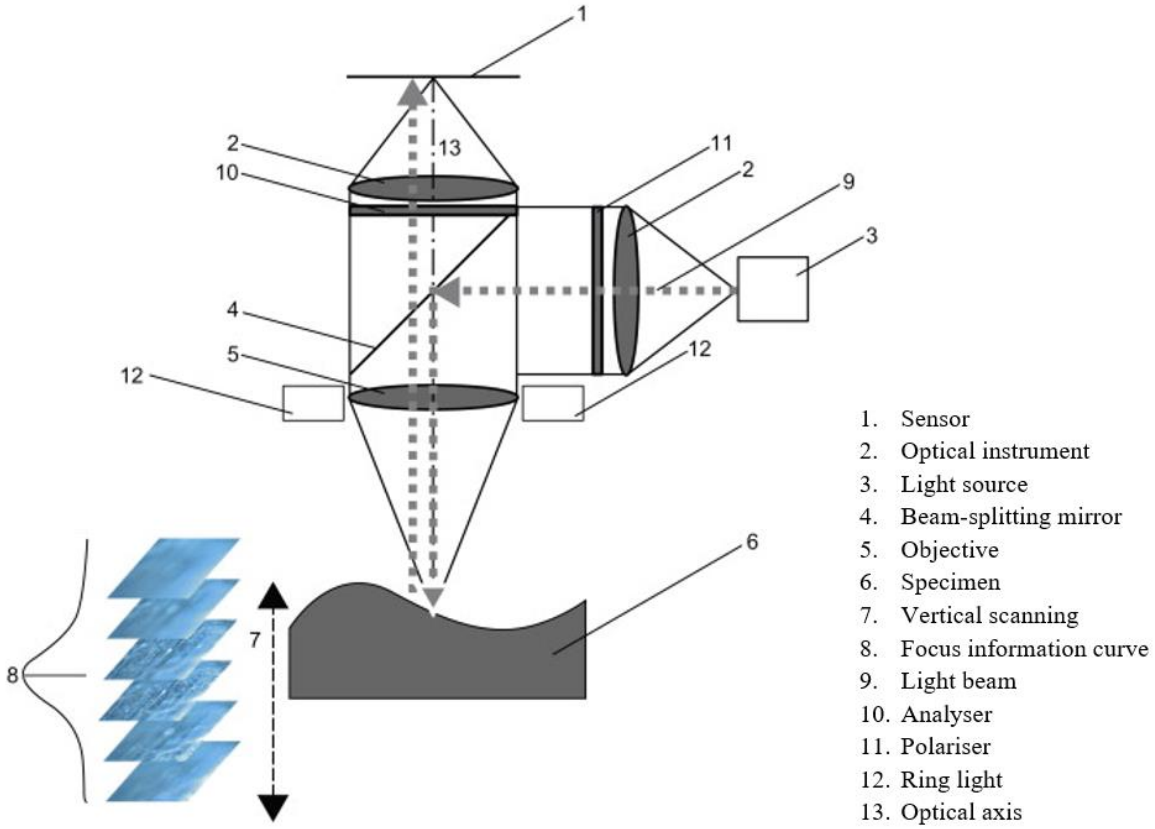

Figure 6: Schematic representation of focus variation [34, p.163], with self-added legend.

The exact method is as follows. Light from the white light source (3) goes through optical path of the system with a beam splitting mirror (4). With the objective (5), the light is focused on the specimen. The topography of the specimen determines the reflectivity of the light in different directions. This reflection can be diffuse i.e. reflected equally in each direction, or specular i.e. reflection mainly in one direction. All the reflected light onto the objective is bundled behind the beam splitting mirror, with the optical instrument (2) and gathered by a light sensitive sensor (1). The optics, however, have only a very small depth of field, so only small regions of the sample give a sharp image. To increase the measurement area i.e. to create a whole scan with full depth of field, the optical arrangement is moved along the optical axis (7,13). This is done while simultaneously capturing date from the specimen. By doing this, each area of the specimen is sharply focused. Next, algorithms can convert the acquired data into a full 3D image and colour image. These algorithms are usually based on a minimum sharpness, so that blurry and out of focus data is discarded, and in focus data is combined [34].

2.2.2 Contact angle

The contact angle (CA) can be measured to characterise the wettability of a material and is the most used parameter for discussing wettability. The CA is the angle between the liquid and the solid surface. This can then be used to predict the wetting behaviour for different geometries or technological processes. A visual representation of the CA is shown in Figure 7 and can be calculated using Young's equation Eq. (2).

$$\cos(\theta) = \frac{(\gamma_{SV} - \gamma_{SL})}{\gamma_{LV}} \tag{2}$$

This equation can be derived by calculating the minimum energy of the system. Here θ represents the contact angle, γ_{SV} the solid surface free energy and vapor, γ_{SL} the surface energy between the solid and the liquid and γ_{LV} the surface free energy between the liquid and the vapour [35], [36].

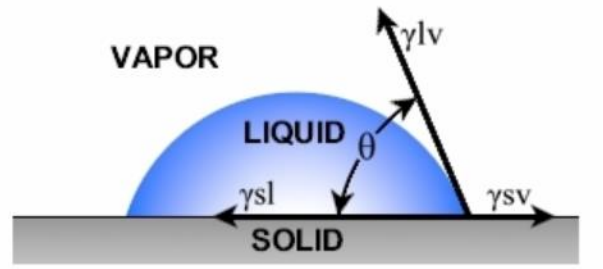

Figure 7: Schematic illustration of the contact angle measurement [37].

The wetting ability of a surface is generally split into multiple categories. The first is the wettable, i.e. hydrophilic category where $\theta < 90°$. When $\theta < 5 - 10°$, it is called superhydrophilic. If the CA is higher than 90°, it is considered hydrophobic, and superhydrophobic if $CA > 150°$ [38]. Some empirical studies however suggest to lower the hydrophilic-hydrophobic border to 65° [39]. These four states are illustrated in Figure 8.

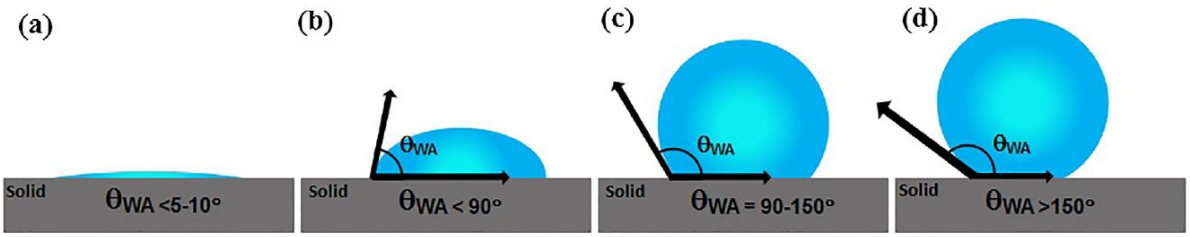

Figure 8: Wetting conditions for a) superhydrophilic, b) hydrophilic, c) hydrophobic and d) superhydrophobic [38, p.4].

2.2.3 Wettability and models

Wetting or wettability is a property of a liquid to maintain contact with a surface. This phenomenon is present in many technologies like painting, printing, filtration, cell and plant growth, medicine and more [40]. The wettability however is determined by two main factors, namely surface energy and surface roughness. The roughness of the surface determines the amount of air trapped in the surface. Air is considered perfectly hydrophobic, because of a CA of 180°, so the more air, the more hydrophobic the surface becomes. Especially hierarchical surfaces, i.e. micro and sub-micro surfaces, can make surfaces effectively (super)hydrophobic [41].
When describing (super)hydrophobicity, two different models, Cassie Baxter and the Wenzel model, as shown in Figure 9, are generally referred.

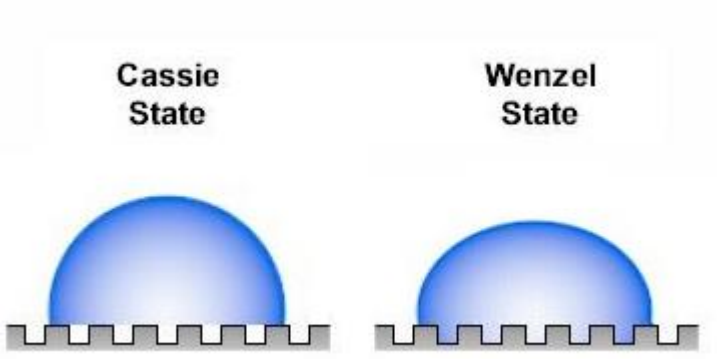

Figure 9: Representation of Cassie-Baxter and Wenzel models [42].

2.2.3.1 Cassie-Baxter

In the Cassie-Baxter (CB) state, the droplet is not in full contact with the surface, because of trapped air pockets. For a correct measurement, Eq. (3) must be used. Here, θ^{CB} is the apparent contact angle, θ the CA from Eq. (2) and $\emptyset_s$ the surface fraction, that corresponds to the ratio of the apparent surface of the substrate and the surface on top of the roughness. Simply put, if depicts the influence of the amount of air trapped in the structure.

$$\cos(\theta^{CB}) = -1 + \varnothing_s(\cos(\theta) + 1) \tag{3}$$

From this equation, it becomes clear that the more air strapped in the surface, the more hydrophobic the structure becomes. This is a confirmation, because as stated previously, air is considered perfectly hydrophobic [39].

2.2.3.2 Wenzel

A droplet in the Wenzel state, is in full contact with the surface, i.e. it penetrates the rough grooves of a texturized surface. Because of this, the actual roughness of the surface must be taken into account, as well as the increase in surface area. For this reason, Eq.(4) can be used, where θ^W represents the apparent contact angle and r the roughness. θ refers to the CA from Eq.(2). In other words, according to the Wenzel model, hydrophobicity is enhanced by greater surface roughness [39].

$$\cos(\theta^W) = r\cos(\theta) \tag{4}$$

2.3 Demoulding of polymers

The replication of micro and nano features using injection moulding is still relatively new. Same as with laser texturing, the functionalised surfaces and parts are still mainly focused on a two-dimensional scale. The research works conducted are focused on the replication of the micro features in the first place.
One of the mentioned advantages of functionalised surfaces on the plastic parts is the reduction and elimination of additives and coatings that can improve the recyclability of the plastics [8].

2.3.1 Micro- and nano feature replication

The injection moulding process is very delicate already. For an optimal processing, a large set of parameters need to be in a narrow range to achieve good products with the desired gloss, texture and colour. These parameters include mould temperature, injection temperature, holding pressure, holding time, material humidity and the injection volumetric flow rate [43]. For micro features, these parameters play a larger role. Because of the micro scale, there is a larger surface area to volume ratio present in these textured areas. This can result in the polymer solidifying to early, and not filling the cavity, and as a result, not reproducing the complete microstructure [5],[44],[45].

The use of a variothermal mould and vacuum venting have been reported in [45] to improve the formation of the micro/nano features. Variothermal and compression moulding have also been reported and proved to increase the reproduced microstructures [5].

Also, the material parameters should be considered. For example, the shrinkage during the cooling and demoulding could affect the resulting roughness of the nano feature because of its small dimensions [46]. Huang [46] also reported that the viscosity is a very important factor to replicate nano features. The higher the viscosity, the higher the tolerance for produced textures. Also, the molar mass proved to be a material parameter than influences the product. In [8], it was proven with two types of PP, with similar shear viscosity, but different molar mass, that there is a difference in the stress relaxation test. The shorter relaxation time of the used PP grade 25 resulted in a better replication quality.

2.3.2 Demoulding of 2D parts

There have been multiple researches to examine ways to improve the demoulding of the resulted parts. One of the examined improvements are coatings on the mould [47]. Here, a CrN coating was applied to study the effect on the produced pillars and the demoulding process, an example of the insert is shown in Figure 10. The coating was not damaged after 6000 cycles, but it reduced the amount of indentations in the pillars, resulting in a better texture. The influence of the demoulding forces has also been studied in [48]. Here it was concluded that higher forces result in a rougher surface. The demoulding force should also always be lower than the yield strength of the material, to prevent deformation of the part.
There have been other examples of successful demoulding of texturized flat parts, like the light-guiding plates in [49].

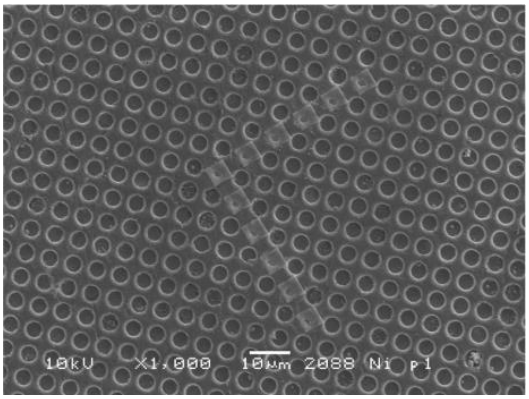

Figure 10: Example of mould insert for PEEK texturized surface [47, p.385].

2.3.3 Demoulding of 3D parts

Very few experiments have been done with three dimensional shapes. Hoppman et al. [50] successfully replicated lenses with a small radius and a micro structure over the whole surface. To achieve these results, a PVD coating was used for the mould. Also, the addition of a variothermal temperature control improved the resulting structure height, to replicate the structure even better. Zhang et al. [51] reproduced a cross shaped parts, with legs under a 60° angle, and micro pillars perpendicular to the legs. This is illustrated in Figure 11. In general, the parts were properly reproduced, with consistent height and diameter of the pillars. There were, however, aspect ratios higher than 1, meaning the pillar was larger than the hole in the mould. These deformations are believed to be caused during demoulding.

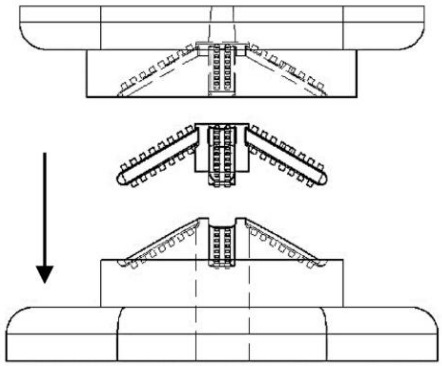

Figure 11: A schematic illustration of the 3D part and mould [51, p.140].

2.4 Corrosion in the nuclear sector

Corrosion sometimes forms problems in range of different sectors, like power generation, nuclear, fabrication, etc. Within the nuclear sector, the corrosion of the structural materials is an important factor for the durability of the installation. Corrosion can lead to a reduction in wall thickness and create activated by-products that can influence chemical reactions. It can also lead to stress corrosion cracking [52].

The usable materials depend mainly on the type of reactor because it decides the working temperatures and the used coolant. For example, there are light water reactors that use water on high working conditions (250°c and 7-14MPa pressure), but there are also lead fast reactors that typically use a special Pb-Bi eutectic alloy. Some materials, like Ni are very soluble with this allow, and thus cannot be used for this reactor. Next there are high temperature gas-cooled reactors, that have an outlet gas temperature above 850°C. This forms a new set of constraints and considerations regarding material longevity and corrosion [52].

2.4.1 Corrosion tests on laser-textured stainless steel

It is very promising to examine ways to reduce the corrosion effect of stainless steels with lasering, because this is the predominantly used materials within the nuclear sector. However, there are not many papers on this, or only with a limited range of structures. Singh et al. [9] examined the influence of the corrosion resistance when femtosecond lasering an array of micro protrusions on a 304 stainless steel. Because corrosion resistance depends on the micro-structure and finish of the surface, this was tested to improve resistance. The corrosion was tested using a 0.5 M H2SO4 + 0.5 M NaCl solution. It was reported that the corrosion resistance of the lasered sample was lower than the original. Some possible proposed reasons include change in oxide film, with a lower Cr/Fe ratio because of the lasering, or precipitation of carbide phase. However, it was explained that because of the increasing hydrophobicity of the sample, there can be an observed corrosion resistance improvement. The sample became highly hydrophobic after 50 days of storage time. With higher hydrophobicity, there is less interaction between the surface and liquid, that can reduce the corrosion speed. Grabowski et al. [10] tested the corrosion resistance when nano- and pico lasering Ti6Al4V alloy, stainless steel and aluminium samples and found similar results of a lower corrosion resistance when using an airy diffraction texture, shown in Figure 12. This texture can be compared with the shape of the waves when a droplet falls on a water surface. The low picosecond laser power densities showed a minimal decrease of corrosion resistance however.

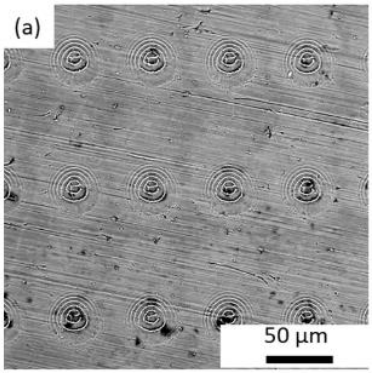

Figure 12: The airy diffraction texture used in Gabrowski's research [10, p.119].

2.5 Laser ablation models

The most common and essential equations used in the laser ablation models are shortly discussed here. Current models for femtosecond ablation are still mainly based on theoretical discussions made from experiments. Especially regarding heating caused by femtosecond irradiation and the change in optical properties for metals that are rapidly heated [18].

The ablation depth is commonly referred to as z and is calculated with the laser fluence according to Eq. (5) . Here is F_{th} the ablation threshold and δ a length with multiple interpretations. This interpretation is dependent on the fluence range. High fluences use thermal parameters like electronic diffusion and interaction time, whereas low fluences use optical absorption coefficient and optical penetration depth [53]. So for femtosecond lasering the optical interpretation is used, because the thermal influences are neglectable [13].

$$z = \delta \ln\left(\frac{F}{F_{th}}\right) \tag{5}$$

The fluence is calculated for a Gaussian intensity profile, according to Eq.(6). Here is F_0 the peak fluence or fluence at the center of the beam, r the radial distance, i.e. the distance from the center to the edge of the beam and ω_0 the beam radius at $1/e^2$of the maximum intensity.

$$F(r) = F_0 \exp\left(\frac{2 \cdot r^2}{\omega_0^2}\right) \tag{6}$$

Another commonly used equation is to calculate the incubation. The incubation incorporates the increase of radiation absorption coefficient because of the increase of defects as a result of consecutive pulses. This is calculated using Eq.(7), with $F_{th}(1)$ the ablation threshold for a single pulse, N the number of pulses and S the incubation factor [19], [53]. Typical values for S range between 0.8 and 0.9 [19]. S equal to one implicates that the ablation threshold is independent of the number of pulses and stays constant [53].

$$F_{th}(N) = F_{th}(1) \cdot N^{S-1} \tag{7}$$

Finally, one more essential equation is needed when talking about ablation. This is the equation for line ablation, i.e. to include a movement of the laser spot. This is Eq. (8) [53]. This is Eq. (5) expanded to be a function of x and y, with Δx the distance between two consecutive pulses.

$$z_k = \delta \ln\left(\frac{F_0}{F_{th}(N)}\right) - 2\frac{k^2 \cdot \Delta x^2}{\omega_0^2} - 2\frac{y^2}{\omega_0^2} \tag{8}$$

3 Materials and equipment

3.1 Sample material

For this research, a stainless steel was used. For the preliminary tests, some left over samples were used, likely being AISI 304 or 316. This was confirmed to be AISI 316, using an XRF measurement at Cel Kunststoffen.

3.2 Sample preparation

For the first samples, no preparation other than cutting them in desired dimensions has been taken. No further surface finishing has been done. This led to Ra values of 0.20 µm and 0.85µm horizontally and vertically respectively.

For further tests, a better finish for the surfaces is recommended. This would limit the influence of the surface roughness greatly. Especially where the lasered grooves are very shallow, the roughness has a possibly large impact on the results.

3.3 Laser processing

For these experiments, a Satsuma Ultrafast Ytterbium femtosecond laser, with a wavelength of 1032 nm has been used. The laser had a 310 fs pulse duration and it was used with its maximum pulse repetition rate of 500 kHz. The average power of the source was 5 W. These parameters were given by the laser research group of Birmingham, because these were the optimised parameters for their laser [14],[25].

Several optical devices were used between the laser source and the sample, as shown in Figure 13. From the laser source, the pulsed laser beam passes through a shutter and a quarter waveplate. This waveplate converts the linear polarised laser light into a circular polarised beam. This beam then passes through a beam expander, where the collimated input beam is expanded. This is done to reduce the beam divergence when transmitting the beam over larger distances [54]. Another reason for using the beam expander is that, when increasing the beam diameter, the actual spot size will get smaller [55]. Finally, the galvo scan head (RhoThor RTA) deflects the beam over the surface.

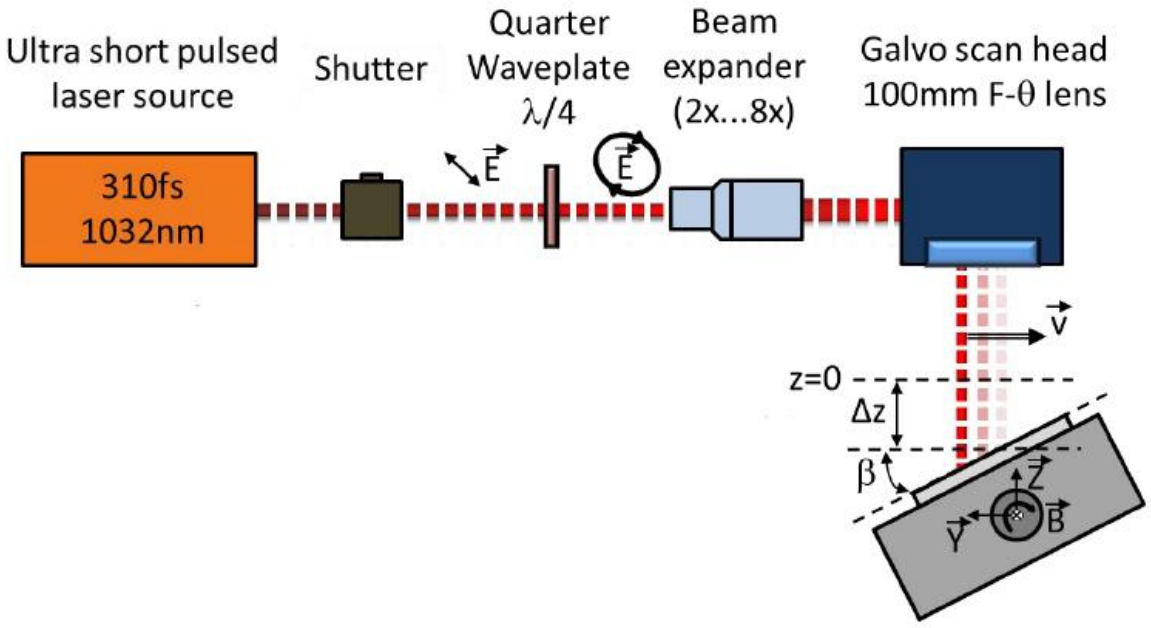

Figure 13: Laser setup and used beam components [56, p.7].

3.4 Characterization equipment and software

3.4.1 Surface equipment

The characterization and scanning of the surfaces have been done with an Alicona G5 measurement system, that is shown in Figure 14. This measurement system used the focus variation technique to create images of the surface. Because of this, Alicona is able to measure both surface roughness and form. Simple measurements are made within a few seconds, which is why this is measurement device is used for a lot of applications. The system is very flexible and accurate as well, with the option to change lenses and lighting type to measure a wide range of materials, structures and scales. Alicona also has a disadvantage however, which is that the created images can contain missing data points, because the surface was too reflective at that location, or an edge was too steep. Sometimes, this can be solved by adjusting lighting parameters.

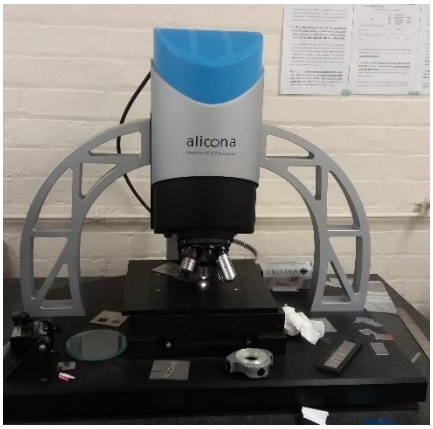

Figure 14: The Alicona G5 measurement system.

To analyse the scans from the Alicona, initially the software "Alicona IF measure suite" was used. Due to circumstances regarding Covid-19, it was impossible to continue using this software, so an open source alternative was needed, and Gwyddion was chosen. Both software packages can be used to extract the profile of the surface from the scans. This profile extraction is then used to determine the desired parameters of the lasered texture.

Because Gwyddion is not Alicona software however, there sometimes is a problem with the missing data. This leads to initial black screens in Gwyddion, because this missing data received unrealistic values when loading in Gwyddion and go up to $3 \cdot 10^{15}\ m$. To solve this, the "limit range" option in Gwyddion should be used, to eliminate this data. In most cases, limiting the data values from 0 to 0.01 % is enough to use these scans as was possible with the Alicona measurement software.

3.4.2 Beam equipment

To analyse the beam shape and dimensions, the Beam'R2 – XY Scanning Slit Beam Profiler has been used [57]. With this beam profiler, it was possible to measure the beam shape, and beam radius in both x and y direction. As defined, this is done by measuring the beam diameter at $1/e^2$ of the peak fluence from the energy distribution, in both directions. The software of the profiler does this automatically and immediately gives the radius.

4 Experimental methods

The main objective is to examine the influence of the disturbances FOD and BIA on a lasered texture. This is combined with the two basic laser processing parameters: the scanning speed and the number of layers, i.e. the amount of laser passes. These parameters were chosen because they are the main processing parameters and determine the total processing speed of the texture. This could then later be used for industrial purposes, to achieve minimal processing times. For example, as described in [17], to incorporate it in a tessellation for 3D CAD models to calculate optimal speeds. Or for certain combinations of process parameters have the same effect on the groove dimensions as another combination, but that has a higher processing speed. The more repetitions, the more total energy is added to the surface and the scanning speed influences the overlap of the beam spot. This overlap is shown schematically in Figure 15 and is determined by the pulse to pulse hatch distance (d) [58]. As the pulse frequency is the same, the scanning speed influences this hatch distance. It can be seen that a higher scanning speed, i.e. a larger hatch distance, the total amount of energy on the surface is reduced as well. To examine both these influences, a simple line geometry as laser pattern is chosen.

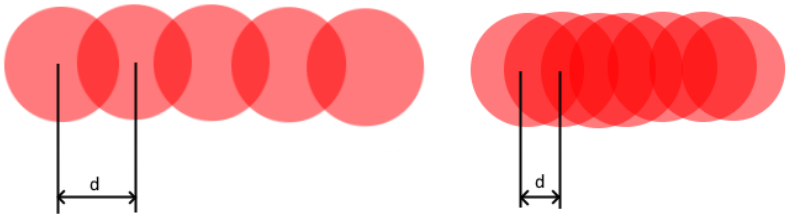

Figure 15: Visualisation of the influence of the pulse to pulse hatch distance (d) and its effect on the overlap. A high scanning speed on the left, and a low scanning speed on the right.

The planned methodology of the experiments is as follows. From a preliminary test set on flat left-over pieces, the first conclusions and remarks are made. This would include certain trends in the groove parameters and remarks like a better surface finish, or larger lasered area. These remarks would be based on the scans made and measured with the Alicona G5. A visualisation in graphs would prove a good way to depict the discovered trends. With these aspects in mind, the test would be redone, on the specified material. These results would be compared to the preliminary set and tested if the incorporation of the remarks improved the measurements. For the next step, a single curved surface is used, and the tests are repeated. If the results are still acceptable, the experiment could be repeated on a double curved surface.

Due to the Covid-19 crisis however, only the preliminary test set was made. So, remarks like reducing surface roughness were not possible to apply. For this reason, certain compromises and measurement approaches were chosen to still properly be able to use this test set.

4.1 Laser texturing approach

To examine the influences of these disturbances combined with the laser parameters, a structured way to laser the samples is needed, so the influences can be studied separately from each other. For the lasering of all the experiments, the maximum repetition rate of 500 kHz was used. Also, maximum power was used what equals to a pulse energy of 7.4 µJ according to Eq. (9). In this Equation, P is the power measured on the actual sample, not the laser source. For the experiments, it was measured to be 3.7W. The f_r is the pulse repetition rate. And all the lasering was done under atmospheric conditions.

$$E_p[J] = \frac{P[J/s]}{f_r[1/s]} \tag{9}$$

As mentioned before, a simple line geometry is used in these experiments. A schematic drawing of such a geometry is shown in Figure 16, and will be referred to as a cell. The distance between the lines is called the hatch. The hatch distance was set on 100 µm for the experiments. The dimensions of one cell were set at 3x1.5 mm, to have enough clearance to make a good scan with the Alicona, even if there was a scratch or debris on the sample. These lines were also lasered perpendicular to the machining grooves present on the sample, to limit the influence of the roughness on the grooves as much as possible.

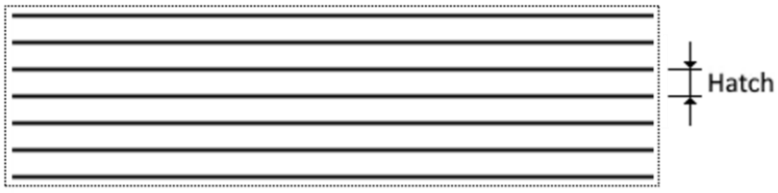

Figure 16: Used line pattern, the horizontal lines are the lasered grooves.

To examine the influence of both laser processing parameters, a matrix or grid like pattern was used. This matrix is built of multiple cells, each where one of these parameters is changed. This is shown on the left in Figure 17. It can be seen that the number of layers (on the x-axis) ranges from 5 to 35 layers. The scanning speed (on the y-axis) varies from 500 to 2000 mm/s. With this matrix, the influence of the laser parameters can be properly examined. A picture of one such matrix is also shown on the right in Figure 17 .

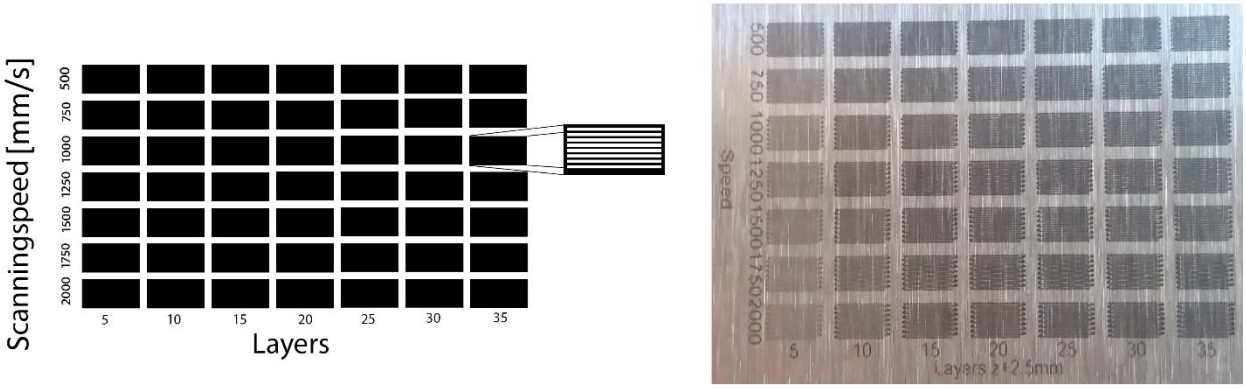

Figure 17: Process parameter matrix for lasering, using the line pattern cells on the left. A picture of a lasered matrix on the right.

To finally examine the influence of the disturbances, this matrix is repeated for different values of the disturbances. For this experiment, a reference matrix was made (FOD and BIA are zero). Then 10 matrices were made with a varying FOD from 0.25 mm to 2.5 mm, in steps of 0.25 mm. The value for the FOD was implemented by first focussing the laser, followed by moving the laser along its z-axis for the FOD value. Finally, 2 matrices were made where the BIA was 10° and 20° with an FOD equal to zero. The same method was used here as well. First focusing the laser, then tilting the mechanical stage for the BIA angle.

There is however an important remark for the BIA matrices. It was not possible to laser a complete matrix at the same time. This would create faults in the automatic focusing of the laser beam. With the default settings, the laser interpreted the change in angle as shown in Figure 18. So instead of setting the whole sample/matrix on an angle, the laser would set each row of the matrix on an angle. This would result in deviations, since the focus of the laser would not be at the sample anymore. To solve this, each row was lasered individually, so the laser projected the texture properly on the sample, as shown on the right of Figure 18. In other words, each row of the matrix was lasered individually, and for each next row, the laser was set back into focus.

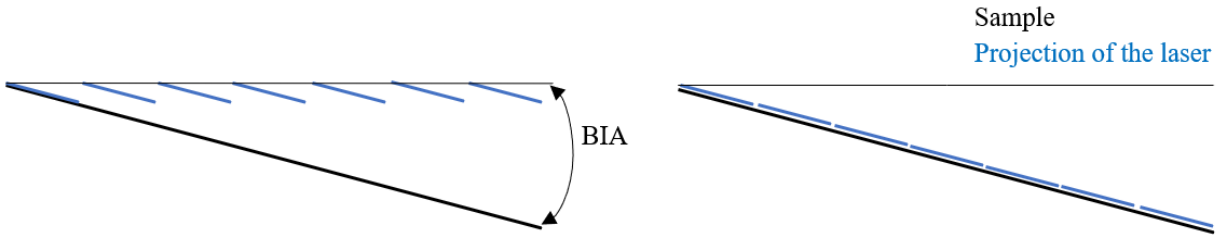

Figure 18: The standard projection of the matrix on the left. The correct and needed projection on the right.

Another remark is regarding the surface roughness. For the preliminary set, there was a visible roughness present on the sample. This would not be a large problem since it was only the preliminary set. This means that, since the texture is a line grid, the lasered lines needed to be perpendicular to the main roughness of the sample. By doing this, the influence of the roughness is kept at a minimum. Because if the grooves were parallel to the roughness, the groove depth would be influenced a lot.

4.2 Peak fluence calculation

To calculate the peak fluence of the laser, a number of steps were taken. First, the beam dimensions were measured using the beam profiler. With these beam dimensions, the area of the beam spot can be calculated, which is then used to calculate the peak fluence.

So first, the beam profiler is used to measure the x and y dimensions of the actual beam spot. This is done for a wide range of values for the FOD. For this test, the range is from -0.9 mm to 2.7 mm FOD, in steps of 0.1 mm. With these dimensions, the area of the beam spot is calculated using the formula of surface of an ellipse, which is shown in Eq. (10). The formula for an ellipse is used because the beam spot was elliptical, not circular. But if it was, then the radius in both x and y direction would be the same anyway.

$$A = r_x \cdot r_y \cdot \pi \tag{10}$$

This area is then used to calculate the fluence or peak fluence. This is done using Eq. (1) and multiplying that value by two, because the peak fluence is twice the normal fluence. The peak fluence is a parameter that is more universal than the FOD. Fluence values can be more easily compared, whereas FOD values do not include important information like the power or pulse duration.

4.3 Measurement approach

The groove parameters of depth and Full Width Half Max (FWHM) are based on the Alicona scans that are examined in Gwyddion. First, the scan is levelled by using the "mean plane subtraction" function. Simply put, this fits a plane to the scan, so a general increase of the height is eliminated. Then, a profile extraction is done to measure these parameters. The extraction is drawing a line (highlighted in red on Figure 19) on the scan, to show the profile of the scan. On this screen, the depth and FWHM can be measured. The average of 5 repetitions is reported in order to get a better representation of the measurements. An important remark for Figure 19, is that the scan seems to have a square hatch, instead of the aforementioned line hatch. The horizontal lines are the laser-processed grooves, the vertical lines are machining grooves, i.e. the surface roughness. In Figure 19, the machining grooves are darker than the laser grooves as the depicted scan is one with very shallow grooves compared to the deep machining roughness.

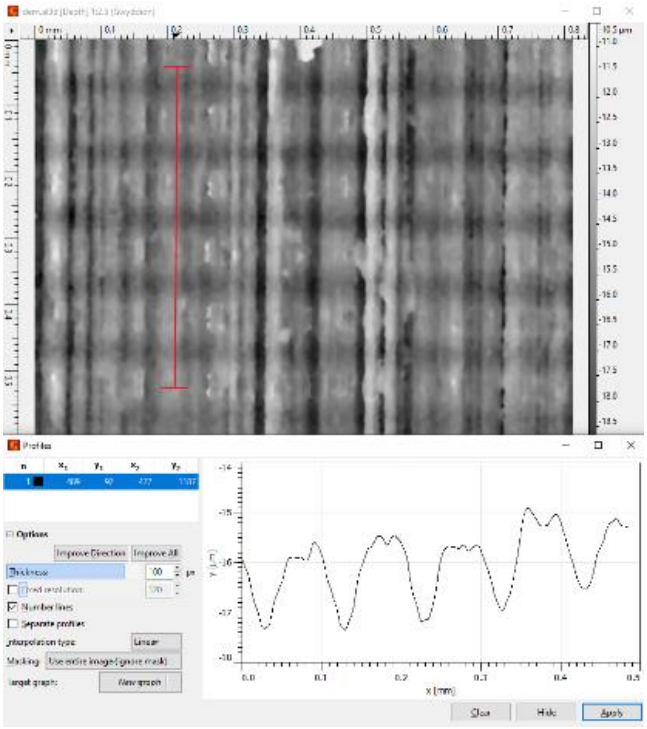

Figure 19: Texture map of a scan. The laser process parameters of this scan are a FOD= 2.25 mm, 25 layers and a scanning speed of 1500 mm/s.

4.3.1 Surface Roughness influence

As mentioned in chapter 3.2, the samples did not have a proper surface finish. Because of this, some considerations had to be made when defining the measurement method. The influence of the surface roughness is the largest where the groove depths are very shallow. In these cases, the surface roughness is almost comparable to the grooves themselves.

In Figure 20, an example of surface roughness is shown. On the left is a scan and profile extraction where the groove around 0.2mm is barely visible. On the right is the same scan, but the profile extraction done on a more even area. More even is intended here as a smoother area, without any vertical machining grooves. In the right image of Figure 20, the grooves are clearer and more regular, what is to be expected since the grooves are lasered in a very structured manner.

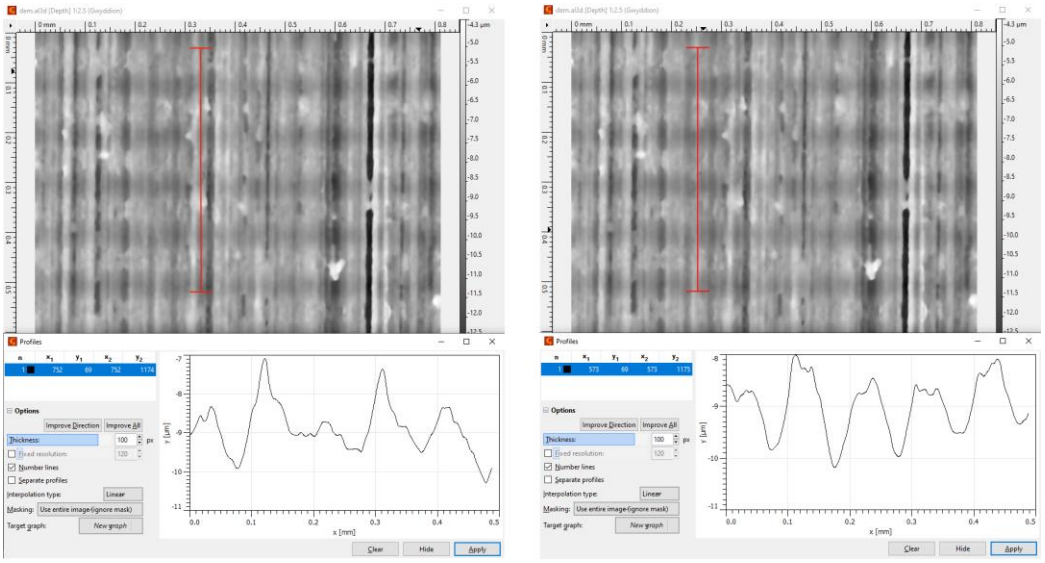

Figure 20: The influence of the surface roughness and the importance of the position for the profile extraction. A bad position where a groove is barely visible (left) and a correct measurement on an even area (right). The laser process parameters are FOD=2.25 mm, 10 layers and a scanning speed of 1500 mm/s.

Another example from this same scan is the influence of a local particle or contamination of the sample. This is also visible on the scan, this time as a very light blob on the image. When making a cross section with this influence present, Figure 21 is the result. Here can be clearly seen that this particle has a large impact on the upper value and is clearly not part of the actual groove. Instead of the 1.5 µm groove depth, this particle gives the fake impression that this right groove would be almost 5 µm deep.

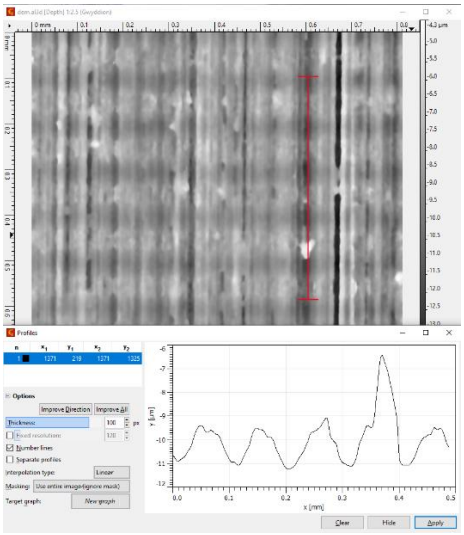

Figure 21: Influence of a particle on a profile extraction.

With both figures, it can be concluded that the placement of the profile extraction is very important for samples with a rough surface. As long as the extraction is done in a smooth area, the influence of the surface roughness is kept at a minimum. It is however a very important aspect to pay attention to, for correct measurements.

4.3.2 Surface roughness values

The surface roughness measurements were done with the roughness tool in Gwyddion. The measurements are shown in Figure 22. The measurements were done only with the roughness tool in Gwyddion, so no dedicated roughness measurement equipment was used. For all these measurements, the Ra and Rz value have been measured. The Ra roughness is the value for which a square with this hight has the same area as the roughness profile of the sample and the average profile. The Rz roughness is the average of independent roughness depth values of five measurement lengths [59]. Both roughness types are shown in Figure 23.

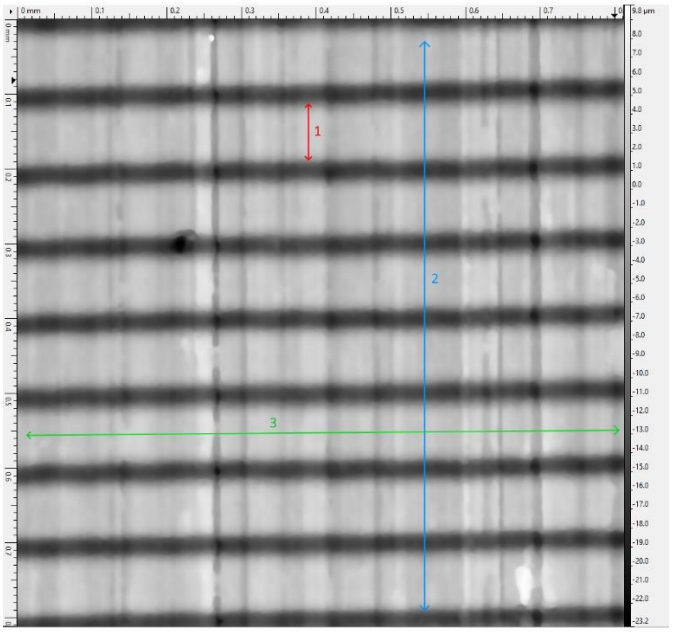

Figure 22: Scan to examine the surface roughness. The red line 1 is perpendicular and between the grooves. The blue line 2 is perpendicular to the grooves and will show the roughness including the groove roughness. The green line 3 is parallel to the grooves and will show the machining roughness.

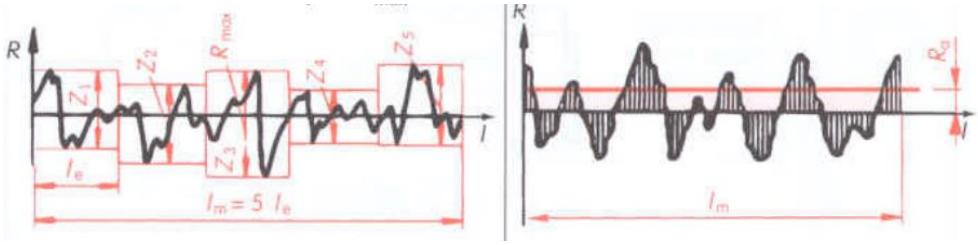

Figure 23: Measuring method for Ra and Rz roughness [60, p.94].

The first measurement is measuring the roughness perpendicular to, and between the grooves. This is done to measure how the roughness could influence the groove shape. This is illustrated with the red line 1 in Figure 22. The reason why only the roughness between the grooves was measured, is because there were only scans filled with grooves. No scans were made without grooves to measure the roughness in this direction. This measurement has been done 30 times in total. 5 measurements each on 4 different scans on the first sample, and 5 measurements each on 2 different scans on the second sample. The measurements on the second sample were done to confirm that the roughness is similar. The average of those 5 measurements will be taken and referred to as Ra-1 and Rz-1.

Other roughness measurements were done across the whole scan, both perpendicular and parallel to the grooves, as shown by lines 2 and 3 respectively in Figure 22. The roughness parallel to the grooves shows the roughness created by machining and without any further surface finish. This was done similarly as previous roughness measurement: sets of 5 measurements of four scans of the first sample, and on two scans of the second sample to confirm similarity. The roughness perpendicular to the grooves, and thus including the grooves themselves, was measured to compare the roughness of the grooves with the roughness of machining. This was measured only in sets of 5 for four scans in total, three on the first sample, and one on the second sample. All these averages are Ra-2 and Rz-2 for the roughness perpendicular to the grooves and Ra-3 and Rz-3 for the roughness parallel to the grooves..

4.3.3 Measurement method

With the influence and remarks for the surface roughness in mind, the actual measurements can be done.

To measure the FWHM in a consistent manner, the used method is as follows. First, the edge of the groove should be determined on the left and the right side. Then, the average height or z-value of these edges should be determined, as shown in red and blue in Figure 24. This is then the upper value, z_{max} of the groove. The next step is taking the minimum or lowest point, z_{min} of the groove. Taking the difference of these two values gives us the depth of the groove Δz, in blue in Figure 24. For taking the FWHM measurement, this Δz should be halved, and added to the z_{min}. At this height, a line should be drawn, and the width should be measured as shown in Figure 24 in orange. This is the Full Width at Half Maximum measurement.
The depth of the groove could be measured at the same time because this is the Δz value used in the FWHM measurement.

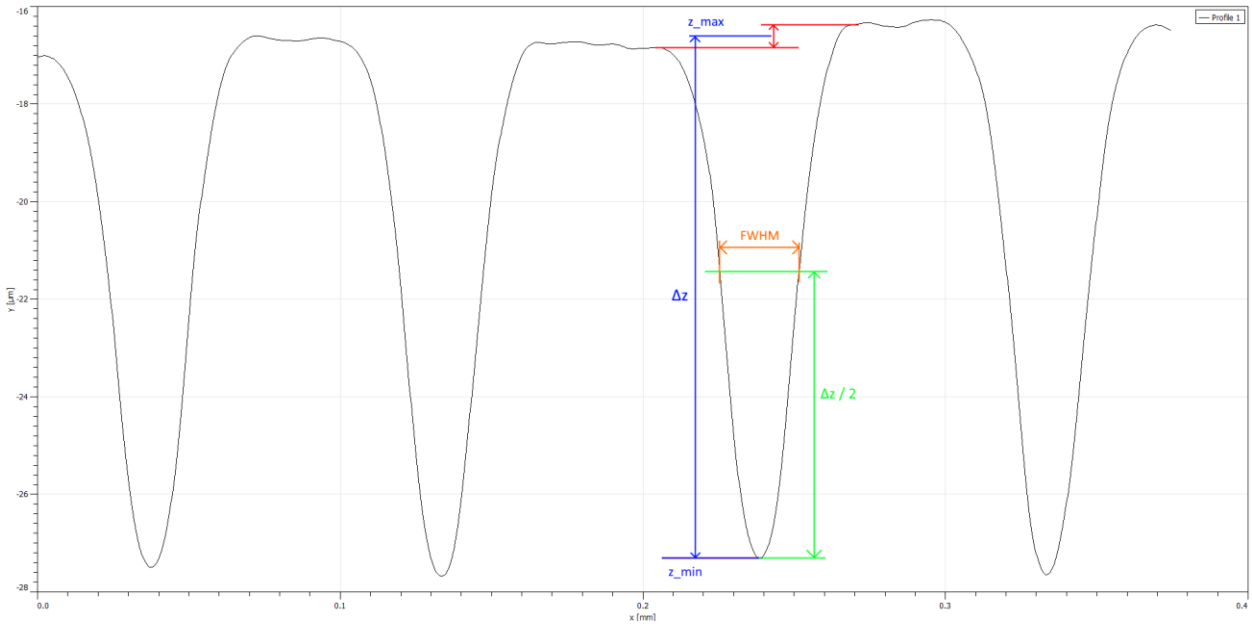

Figure 24: Measurement method for groove parameters. Step 1 in red: selecting the edges of the groove. Step 2 in blue: defining the groove depth. Step 3 in green: a line at half depth. Step 4 in orange: measuring the FWHM at intersecting points.

The reason for this measuring method is because the shape of the grooves can change depending on the user parameters and disturbances. Figure 25 shows this change. On the left, grooves made with the laser in focus, i.e. a higher fluence, are shown. Here, the horizontal grooves are very clear and distinguishable from the

vertical machining grooves. The profile extraction shows a profile similar to Figure 24. On the right side however is a scan made with a high FOD, i.e. a lower fluence. Here, the grooves are not as clear on the scan, especially since there are 2 very visible machining grooves present. As for the profile of this scan, the grooves are visible, but they are not as repetitive as the profile on the left. This is mainly because the surface roughness is much larger in proportion to the groove depth than the scan in focus. This is also visible in the area between the grooves. On the left, the area is almost completely flat, whereas on the right, there is a certain wave shape present and visible because of the roughness. Because of the difference in groove edge, most clear for the second groove of the left image, this way of measuring was chosen to be able to measure the groove dimensions in a consistent manner.

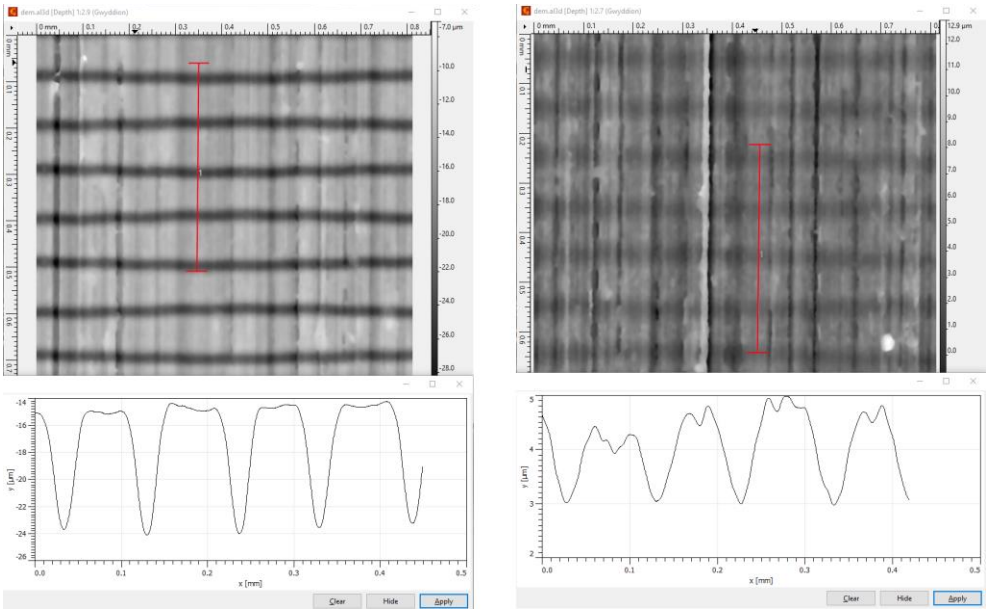

Figure 25: Comparison of scan and profile in focus and further out of focus. The scan on the left is made in focus (FOD=0), 15 layers and a scanning speed of 1250 mm/s. The scan on the right is made at FOD= 2 mm, 20 layers and a scanning speed of 1750 mm/s.

4.4 Laser ablation modelling

In addition to the experiments, some modelling has also been done. The model was provided by KU Leuven and is based on [61] and [62]. It is a simple model to calculate the ablation depth for femtosecond lasering, based on the main equations (5-8). Some of the assumptions made in the model will be mentioned, because these are important to take into consideration.

4.4.1 Model parameters

Before discussing the assumptions and simplifications of the model, the model parameters will be discussed. The modelling is performed though Python scripting and Figure 26 shows the model when run in Spyder, IDE for executing Python scripts. When choosing the processing option and polarisation method, the required input parameters can be filled in. The result of a calculation is an ablation profile as shown in Figure 26.

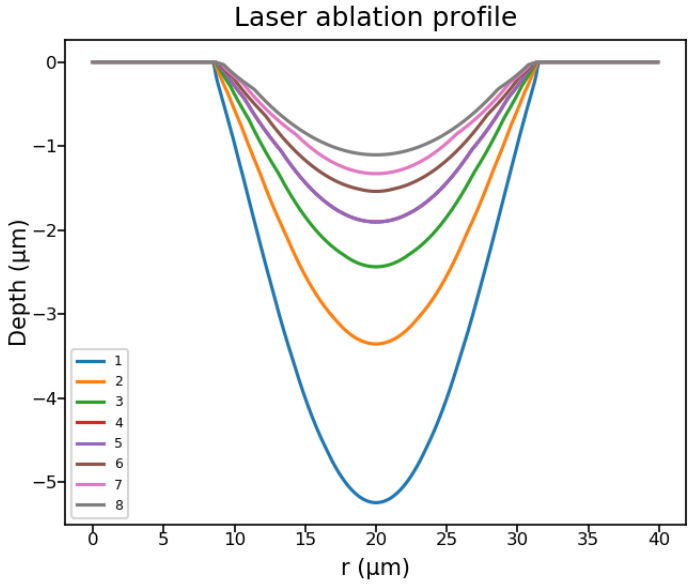

Figure 26: Example of calculated ablation profiles from the model.

Only the parameters needed for the “Area” process will be discussed, as this is the option to model a line hatch. The parameters are listed again in Table 1. The used values are next to the parameters, each having a specific colour. The colour represents how certain each value is deemed. Green values are very certain, because these are fixed parameters of the laser, or self-set values for processing, e.g. the scanning speed. Blue values are material specific values, and as such should be fixed. But since laser ablation can influence the material parameters, like reduction of the ablation threshold or reflectivity that changes when ablating the top layer (with possible corrosion or debris), these are put into a separate category. Finally, there are the red values that are less certain. These values could be finetuned further in future research. This is especially the case for the penetration depth and incubation factor. For the beam radius, different values have been used, as will be explained later.

Table 1: The model parameters with their basic values used.

Ablation Threshold [J/cm²]	0,32
Penetration depth [nm]	27,5
Incubation factor	0,8
Pulse Energy [µJ]	7
Beam focus radius [µm]	19,4
Pulse repetition rate [Hz]	500 000
Laser wavelength [nm]	1 032
Scanning speed [mm/s]	1 000
Number of lines	1
Line pitch [µm]	100
Number of layers	5
Reflectivity [%]	0

The ablation threshold is the lower limit of the fluence to be able to ablate the material. It should be noted that this is the single pulse threshold. The optical penetration depth is a measure to show how deep an electromagnetic wave or radiation (like light) can penetrate the material. For femtosecond lasering, this optical effect is predominant to the thermal effects [30]. The incubation factor is the parameter that implements the change in ablation threshold because of the consecutive laser pulses. The pulse energy is the energy of a single pulse on the sample, calculated using Eq. (9). Next, the beam focus radius is the radius of the laser beam. This influences the area of the beam spot, and thus the fluence. The pulse repetition rate is the frequency of the laser beam, i.e. the number of laser pulses per second on the sample. Then, the laser wavelength is generally a completely fixed parameter, because this depends on the laser source. Furthermore, the scanning speed is the speed at which the laser spot moves over the sample. For the experiments, this was one of the main adjusted parameters. The number of lines is a model parameter that only influences the visual presentation. It changes how many grooves are drawn in the graph. The number of layers however is the second varied parameter. This determines the number of times the laser passes of the groove. And finally, the reflectivity is a material parameter to vary the reflectiveness of the sample.

For this study, only the beam focus radius, scanning speed and number of layers have been varied. Because there is a difference between the radii, all three radii are checked and used for the model. The laser parameters were the same as the ones used in the experiments. The other values have been taken over from the literature [19],[63],[64].

4.4.2 Model measurement method

Because the model itself has no option to give the numerical values of the depth, a different method to measure the model values has been followed. For these measurements, a screenshot of the model has been taken (similar to Figure 26) and printed on a piece of paper. Then the measurements were done by hand on the paper, as described in chapter 4.3.3. This was only done once for all the values. Because the scale is also present on the printed figure, it is used to calculate the actual depth and FWHM and this was added to the worksheet.

4.4.3 Model assumptions

The used model for this paper is a simple femtosecond irradiation model. The model has only been checked to see if has the same results when having the same process parameters used in [18] and [19]. One of the assumptions and simplifications lies with the irradiation part. This means that the model does not take into account the thermal changes of the material. For femtosecond lasering, the thermal impact is significantly lower than for nanosecond lasering. There still are thermal influences however, especially for certain process parameters, like low scanning speed and/or large number of layers. With these parameters, a heat build-up can still occur.

Secondly, the model assumes a perfect circular Gaussian beam. However, the beam is never perfectly Gaussian or circular. That is why for example the M^2 value is important when describing lasers.

Because of these assumptions, the ablation profile is only calculated from the optical penetration depth, ablation threshold and fluence. In other words, it does not include material, beam or surface imperfections. This is why the model does not take into account imperfect beam spots

Other than this, the internal reflection is not taken into account. When there are multiple pulses on the same spot, the surface is not flat anymore, which results in an uneven geometry. This change of geometry will change the reflectivity of the surface and will become more internal.

Another aspect that is neglected is the so called “first stage” of a laser pulse. This refers to the rising edge of the laser pulse where the electrons of the metal are heated rapidly to the Fermi temperature. Here the relaxation time of the electron decreases with increasing temperature. By neglecting this for the model, electron thermal diffusivity, the heat capacity, and the thermal conductivity can be considered constant [18].

5 Results

A general remark for all the graphs is that all the used margin or errors are calculated from the standard deviation. This is then recalculated to achieve a 95% reliability. These values are used as the margins.

5.1 Peak fluence

Figure 27 shows the calculated peak fluence as function of the FOD values. The peak fluence was calculated using Eq. (1), multiplied by 2. Here it can be clearly seen that an increase in FOD results in a lowering of the fluence. This is because of the area increase with increasing FOD, and thus, a lowering of the energy density or fluence.

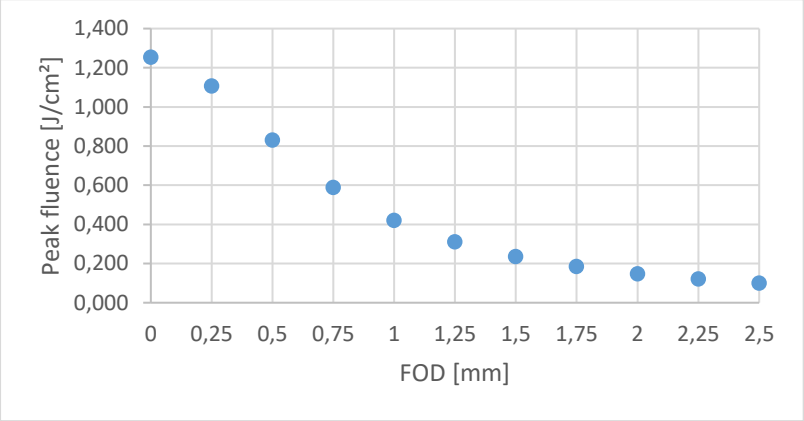

Figure 27: Progression of peak fluence compared to FOD values.

It is also shown that the peak fluence values around 1-1.25 mm lie around the ablation threshold of the stainless steel (0.32 J/cm²) for single pulse ablation, provided from the literature [63]. This can also be seen when plotting the predicted groove depth as function of the fluence in Figure 28. This shows that when the peak fluence is close to, or lower than the ablation threshold, the groove depth decreases drastically. When the peak fluence is high enough, the lowering of the ablation threshold by having multiple pulses helps the ablation process. Compared to when the peak fluence is very low, this lowering of the threshold becomes the main cause for the ablation. The ablation threshold can possibly be calculated from Figure 28. This can be done by plotting a trendline on the data and extrapolate for which fluence the groove depth would be zero. This has been done in Figure 29. A logarithmic trendline was used, to fit the datapoints as best as possible. The equation shown in the figure was used to calculate for which peak fluence (x) the groove depth (y) would be zero. This was calculated to be a peak fluence of 0.0468 J/cm² and is very low compared to the one provided in the literature of 0.32 J/cm² for single pulse ablation.

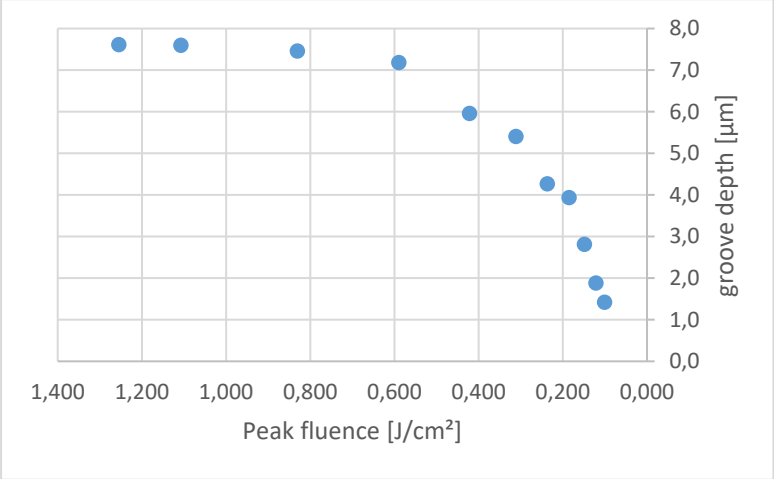

Figure 28: Predicted groove depth as function of peak fluence. Process parameters of 5 layers and 500 mm/s scanning speed.

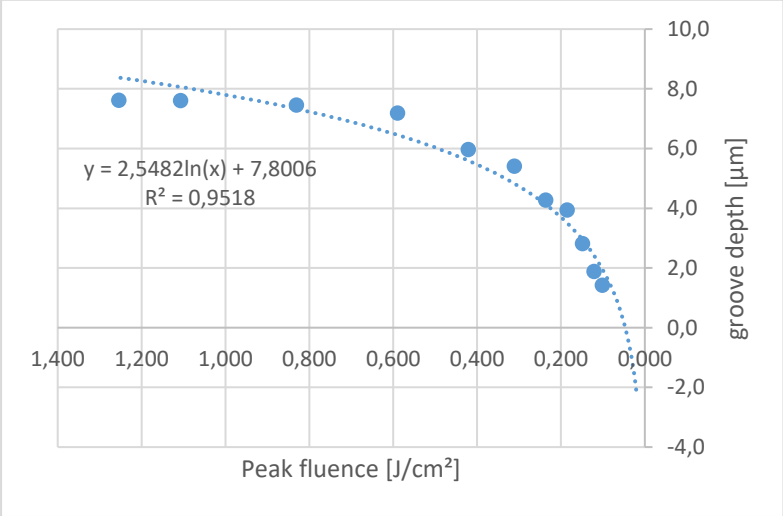

Figure 29: Predicted groove depth as function of peak fluence, with trendline to calculate possible ablation threshold.

5.2 Surface roughness

When executing the roughness measurements as described in ch 4.3.2, the values shown in Table 2 are achieved. First of all, the Ra roughness between the grooves (Ra-1) lie very close to each other, around 0.2 µm. Only the first sample has a slightly lower roughness. It can still be concluded that the roughness between the grooves is very similar and relatively small when comparing to roughness values achieved by processing [59]. Similarly, when comparing the roughness parallel to the grooves (Ra-3), these are also close to each other, around 0.9 µm. This roughness was expected, since this is a very likely roughness for normal machining processes, like cutting, drilling, etc [59].

However, when comparing these values to the roughness perpendicular to and including the grooves (Ra-2), some interesting remarks must be made. First of all, as expected, the roughness increases when lasering the grooves on the sample. The amount of layers and FOD have an influence as can be seen in Table 2. Especially when looking at the depth values of the grooves, this trend is expected, because of lower added energy and thus lower depth. When comparing both roughness values perpendicular and parallel to the grooves, it can also be seen that with this lower energy, the roughness including the grooves is almost the same as the machining roughness. This confirms that the mentioned measuring method of only drawing

profile extractions on even areas is necessary. This also shows that a better surface finish might improve the experiments, because there is a not neglegible machining roughness from the beginning. Even for scans with a high energy, e.g. 35 layers at 0.25 mm FOD, this machining roughness is still around 20-25% of the finished laser roughness.

Table 2: The roughness values measured with Gwyddion of the different samples.

Sample	Ra-1 [µm]	Rz-1 [µm]	Ra-2 [µm]	Rz-2 [µm]	Ra-3 [µm]	Rz-3 [µm]
0 FOD , 5 layers, 2000 mm/s	0,15	0,50	0,71	2,72	0,88	3,89
0 FOD , 35 layers, 1250 mm/s	0,24	0,77	/	/	0,93	5,16
0.25 mm FOD, 35 layers, 1250 mm/s	0,20	0,58	3,67	12,57	0,88	4,34
0.5 mm FOD, 25 layers, 1000 mm/s	0,21	0,87	3,59	12,55	0,96	3,59
1.75 mm FOD, 10 layers, 1500 mm/s	0,20	0,46	0,86	2,44	1,04	3,79
1.75 mm FOD, 30 layers, 750 mm/s	0,23	0,63	/	/	0,95	2,35

From this table can be concluded as well that, the strategy for lasering the line hatch perpendicular to the machining grooves was the correct laser strategy. If this lasering was done parallel to the machining grooves, the largest roughness would most certainly influence the cross section of all the grooves, whereas now this influence is limited as much as possible for these samples.

5.3 Beam measurements

When examining the beam with the beam profiler, it was found that the beam spot was elliptical in shape, not circular. This is frequently the case for astigmatic beams, i.e. beams with waist positions at different positions [65], but should be taken into account. Not only this, but the radii of the ellipse (r_x and r_y) changes differently when changing the FOD. This is shown in Figure 30. The difference in trend for both radii could be explained by the fact that the laser beam has a small difference in M^2 value in both the x and y direction. There is a third radius in this Figure. This is the equivalent radius r_{eq} that is calculated using Eq. (11). It is the radius of a circular spot that has the same area as the elliptical beam.

$$r_{eq} = \sqrt{r_x \cdot r_y} \tag{11}$$

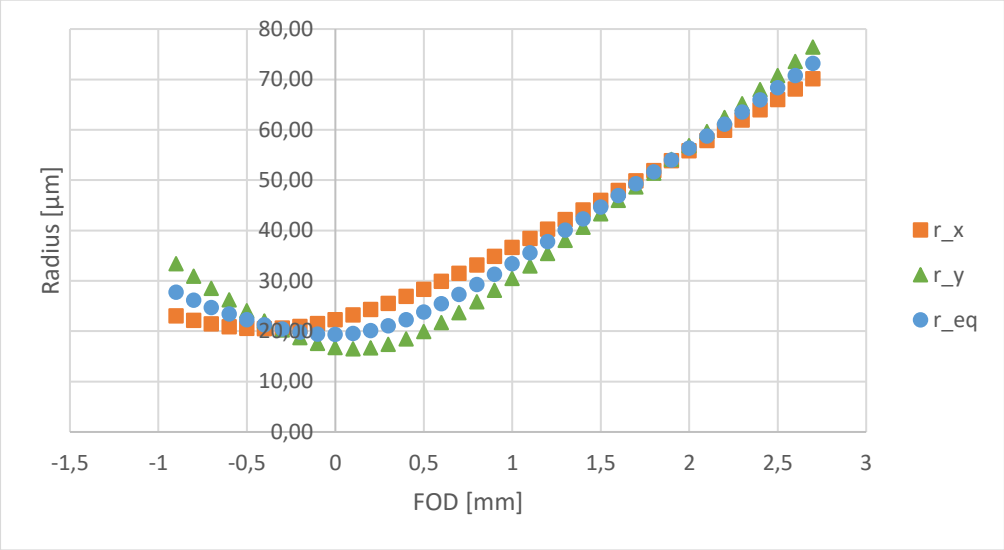

Figure 30: The different radii used in the model. r_x and r_y from the beam profiler and r_eq calculated

5.4 Experimental results

5.4.1 Influence of scanning speed and layers

Before examining the influence of the disturbances, the influence of the processing parameters (scanning speed and number of layers) is examined. Figure 31 is then achieved where there were no disturbances present.

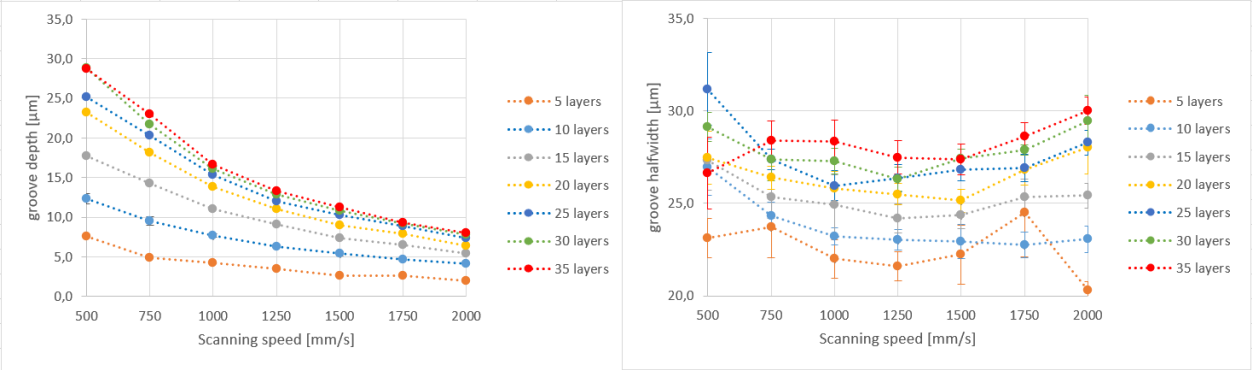

Figure 31: Influence of scanning speed and number of layers on the depth (left) and FWHM (right) of the grooves, without disturbances present.

It can be seen from Figure 31 that, an increase in scanning speed decreases the depth of the laser grooves. This is mainly because of the decrease in overlap with higher scanning speeds. This reduction in overlap lowers the total amount of energy added to the surface to create the grooves.
Somewhat similarly is that, when increasing the number of layers, the groove depth increases. This is because when adding more layers, the amount of energy added to the surface is increased. It is also shown that both parameters exist next to each other. For example, when comparing 500 and 2000 mm/s scanning speed, the influence of the increased number of layers is still present, even if the actual effect on the grooves is reduced.

When looking at the FWHM, some different conclusions can be made. First of all, it can be seen that the margin of error is larger than with the depth measurements. While doing the measurements, it became clear that the width of the grooves varied more between grooves than the depth. Secondly, the influence of the scanning speed seems to be very minimal. The FWHM seems to be somewhat constant with varying scanning speed. This can be explained by the fact that an increase in scanning speed lowers the overlap of the beam spot as seen in Figure 15. A decrease in overlap however does not mean the dimensions of the beam spot changes, and so, the width stays the same. Finally, the number of layers does have an influence on the FWHM of the grooves. In general, the more layers added, the wider the groove. This is caused by the increase of passes of the laser. At the edge of the beam spot, the fluence is very low, but because of the multiple repetitions, the grooves can become wider.

5.4.2 Influence of FOD

When examining the influence of the FOD, or Focal Offset Distance, it is important to verify that all the values are from the correct set of laser parameters. For these tests, the four corners of the matrices were examined. In other words low scanning speed (500 mm/s) with low layers (5), high scanning speed (2000 mm/s) with low layers (5), high scanning speed (2000 mm/s) with much layers (35), and low scanning speed (500 mm/s) with much layers (35). These are shown in Figure 32.

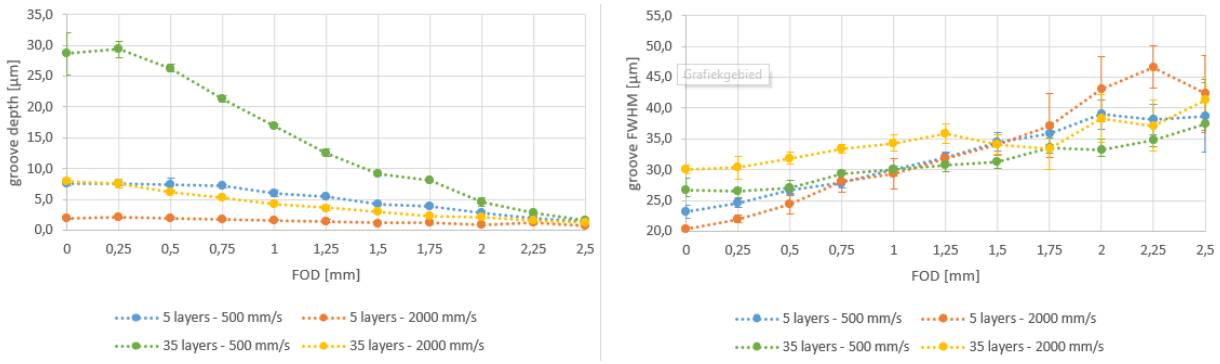

Figure 32: Influence of the FOD on the depth (left) and FWHM (right) of the grooves. Processing parameters of 5layers- 500 mm/s, 5 layers- 2000 mm/s, 35 layers- 500 mm/s and 35 layers- 2000 mm/s.

When increasing the FOD, the depth of the grooves clearly decreases. This is mainly caused by the decrease of peak fluence with increasing FOD, as is shown in Figure 27. It should also be noted that without a FOD disturbance present, the difference in depth is large. This is especially the case when comparing similar number of layers with each other. However, with the increasing value for FOD, this difference becomes smaller, to the point that at a FOD of 2.25 and 2.5 mm, the difference is nearly zero. This leads to the fact that a high FOD value overthrows the earlier conclusions regarding scanning speed and number of layers. Even though a FOD of over 2 mm is very rare, this still shows the possibly large influence of a Focal Offset Distance.

To examine the influence of FOD for the lower depth values, the measurement of 35 layers- 2000 mm/s was excluded, to create Figure 33. Here it can be seen that for the lower values, the same lowering of the depth applies. Interestingly, the depth of the blue and yellow curve is very similar, especially for little to no FOD present. This leads to interesting possibilities for industrial uses of the laser. Namely that the depth is similar with completely different processing parameters. 5 layers at 500 mm/s have the same result as 7 times as much layers, but at 4 times the speed. This can be used in combination of the processing time calculation, to utilise the laser to its maximum potential. And as expected, the orange curve (5 layers – 2000 mm/s), has the lowest depths. This is because these parameters give the lowest total energy to the surface. Namely, the lowest number of layers is combined with the highest speed, i.e. the lowest overlap of the beam spot.

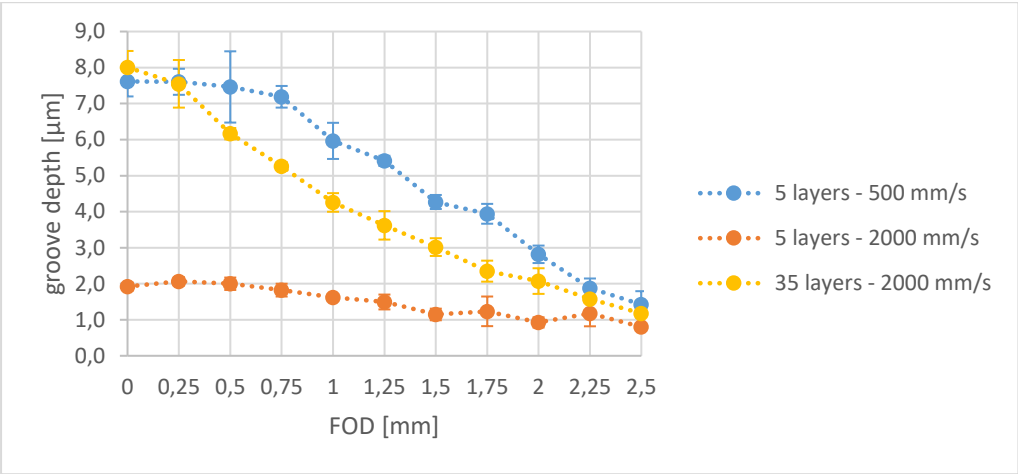

Figure 33: Influence of FOD on depth, without the 35layers - 2000 mm/s measurement.

For the FWHM, it is also shown (Figure 32) that there is an influence because of a FOD. In general, a higher FOD results in wider grooves. This is because with an increase in FOD, the beam dimensions increase, as mentioned before. These increased dimensions lead to a larger beam spot, and thus, a larger lasered surface and grooves. It should again be noted that for the FWHM measurements, the margin of error is large, because of the groove shapes. Especially for the orange curve (5 layers – 2000 mm/s) the margins are especially large, because this is the laser setting with the lowest added energy to the surface. This led to very shallow, irregular and difficult to measure grooves sometimes.

5.4.3 Influence of BIA

Finally, the influence of the BIA or Beam Incident Angle was examined. This influence is shown in Figure 34. Here it can be seen that, for the limited angles examined, the depth is greatly influenced for some processing values. From these results, it looks like the depth is greatly affected when a BIA is present, but further increase of the angle has little effect. The FWHM also sees a change with the introduction of an incident angle.

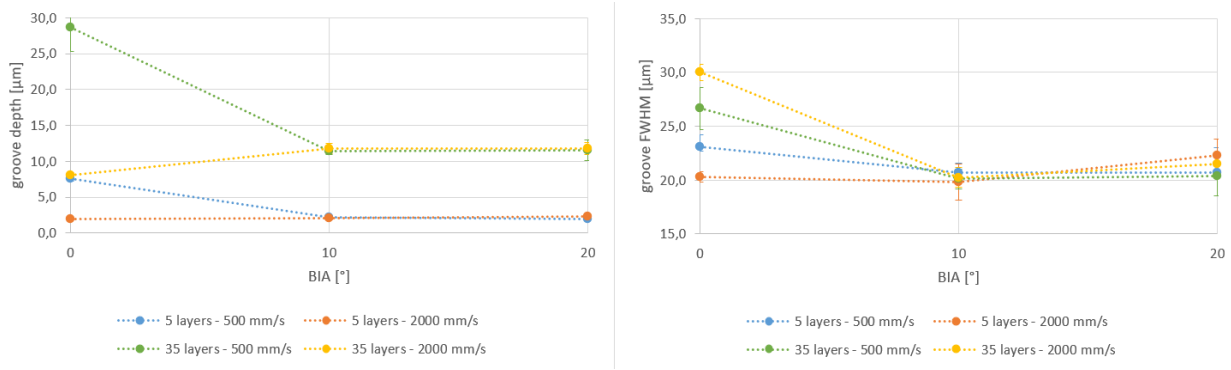

Figure 34: Influence of BIA on depth (left) and FWHM (right). Processing parameters of 5layers- 500 mm/s, 5 layers- 2000 mm/s, 35 layers- 500 mm/s and 35 layers- 2000 mm/s.

For the groove depth, the BIA seems to have a strange effect. Unrelated to the scanning speed, the depth converges to a set depth value when a BIA is introduced. This is the case for both 5 and 35 layers. For both number of layers does the fast speed (2000 mm/s), i.e. lower depth, increase to this depth value. The red and

yellow curve in the figure have a slightly lower depth before the implementation of a BIA than when a BIA is present. The low speed on the other hand (500 mm/s), i.e. higher depth, decreases to the BIA depth value. Like the green and blue curves show. The number of layers however does have an effect on the depth with a BIA value.

Similarly, for the FHWM of the grooves, there is a convergence when introducing a BIA. In this case however, there is no difference between the number of layers or the scanning speed. All the grooves converge to the same FWHM. With the larger margin of errors for the FWHM, also for BIA = 20°, the measurements can be at the same value.

When comparing the influence of the scanning speed and number of layers when there is a BIA or not, a peculiar trend is shown in Figure 35. Here it can be seen that the presence of the BIA overshadows the previous conclusions of a decrease in groove depth when increasing scanning speed. The groove depth appears to be constant when increasing the speed. At the same time, the groove depth appears to be at the lower end compared to when there is no incident angle present. The almost constant depths with BIA = 10° correspond very closely to the depths at scanning speed = 1500 mm/s without an incident angle.

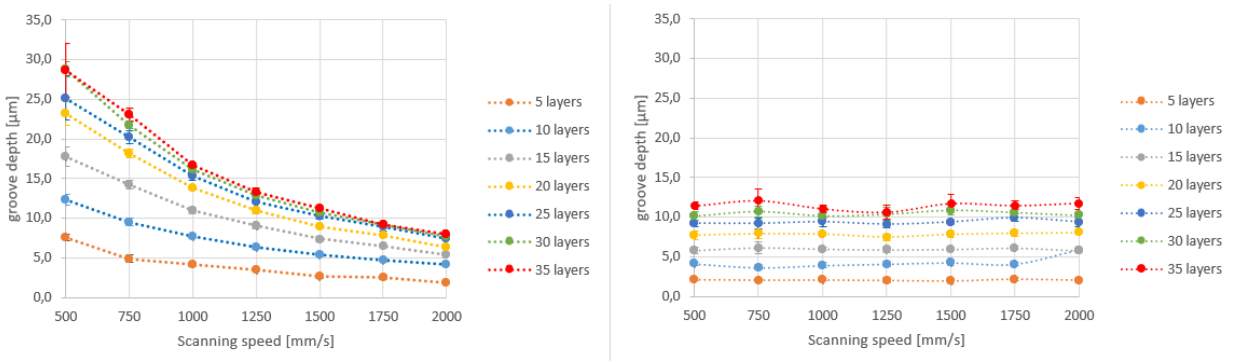

Figure 35: Comparing the influence of scanning speed and number of layers on groove depth at different BIA values: 0° on the left, and 10° on the right.

It must be noted that a more detailed examination of the BIA should be done. As the results indicate, the change in groove parameters is very large when going from ideal to an BIA of 10°. Further tests should be conducted with smaller changes in BIA, e.g. in steps of 2° from 0 to 10°, to confirm that any incident angle has an effect, or if there is a more gradual decrease between 0 and 10°.

Another very important remark must be made however. The measurement method mentioned in chapter 4.3.3 might explain the strange progression of the BIA results. As Figure 36 illustrates, both the cross section and shape of the grooves change slightly when introducing a BIA. The groove become less symmetrical, and slightly tilted. The measurements on this figure illustrate this. With an increasing BIA, the lowest point of the groove no longer lies in the middle of the groove. It must be noted that the grooves are drawn at the same scale in this Figure 36. By using the same scale in the depth direction, it can be seen that de groove depth decreases in case of a BIA.

Because of the symmetrical shape for BIA = 0°, the FWHM measurement gives very consistent values. But as the grooves become more asymmetrical, the consistency decreases. Attention should be paid, especially when comparing these values with each other. Comparing values with the same BIA will have less problems, because all the measurements were done on the same asymmetrical grooves. A possible reason for the

differences is that with a BIA different from 0°, the depth is measured perpendicular to the surface, instead of the groove itself. Especially for higher values of BIA (not tested in this research), will result in different depth measurements. This must be considered when comparing these values.

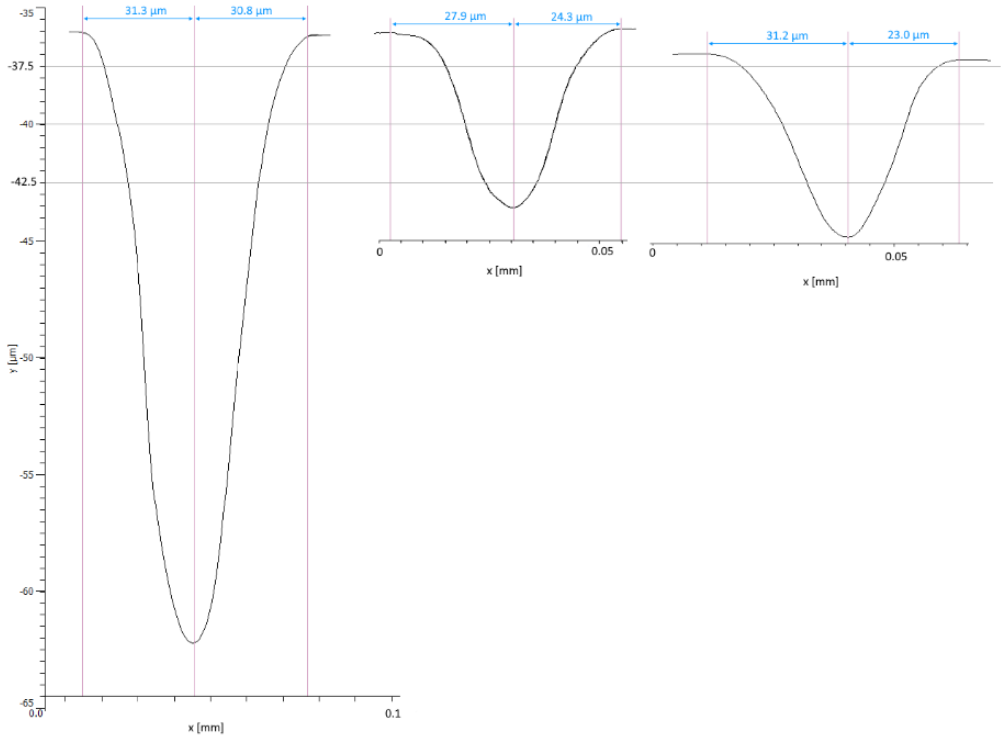

Figure 36: Grooves at different values for BIA. Laser parameters of 25 layers and 500 mm/s scanning speed, with BIA of 0°, 10° and 20° from left to right respectively.

The normalised difference between the distance from the left and right edge to the middle has been examined. Table 3 shows the results that are calculated with Eq. (12). L represents the left distance, and R represents the right distance. This was done for 20 different grooves for each BIA value. Here the percentage is shown much larger the left distance is compared to the right distance. Figure 37 indicates the incident direction of the beam. Table 3 shows that for a larger BIA, the left distance does increase compared to the right distance. There is also a large margin of error present, this time calculated only with the standard deviation. The increasing margin of error is caused by the upper part of the grooves increasing, i.e. becoming wider, as can also be seen in Figure 37. This increase causes a more diverse range of groove edges, and makes them less consistent.

$$\frac{L-R}{R}\cdot 100 \tag{12}$$

Table 3: The normalised difference of the left side of the groove compared to the right side, caused by a BIA.

	BIA 0°	BIA 10°	BIA 20°
Left half larger than right halve [%]	1 ± 5 %	8 ± 7 %	20 ± 10 %

When further examining the asymmetry of these grooves, it was a question if the BIA was visibly present in these grooves. An attempt to measure this has been taken and seen in Figure 37. Here, the average of the edge heights was taken (the green lines), similarly as used for the measurements for the depth and FWHM of the experiments. Then, the actual middle of the groove, at the top, was calculated, by taking the average of the left and right value. This actual middle is the orange dot in the figure. Then a line from this middle, to the lowest point of the groove was drawn, and the angle between the vertical and newly drawn line was measured. As can be seen, this difference is not as large as the BIA, since the angles lie around 3 and 5° for a BIA of 10 and 20° respectively. So this influence is less visible as initially expected. It should be noted however, that a BIA of 15° was tested in [53], for 500 mm/s scanning speed and 500 passes with a peak fluence of 2.9 J/cm². For this experiment, the inclination of the beam was much more visible, and more similar as would be expected. A possible explanation lies in the higher energy for this test, compared to the experiment done for this research. Both the peak fluence and the number of passes is much higher. The result of 15° test is shown in Figure 38 as comparison. It should also be noted that tis test was executed on polished stainless steel 316L samples.

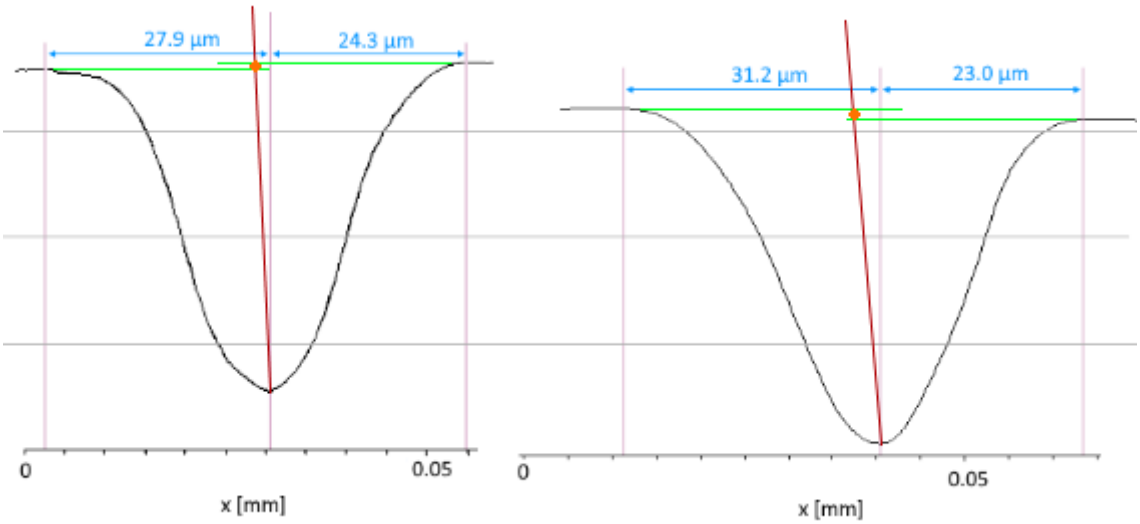

Figure 37: An attempt to see if the BIA is visible in the shape of the groove.

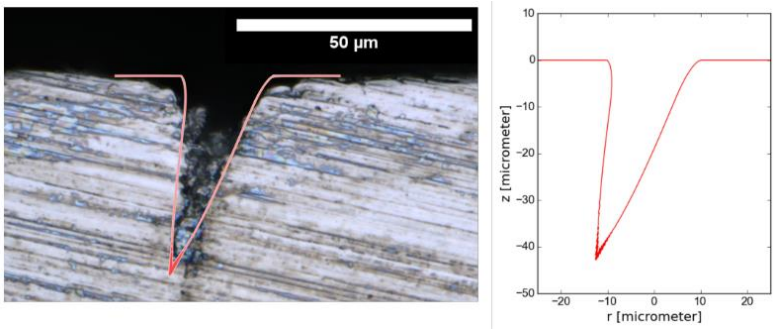

Figure 38: The result of a BIA of 15°, with 500 mm/s scanning speed, 500 passes and 2.9 J/cm² peak fluence [53, p10].

5.4.4 Expectations for complex surfaces

Because the initial theme of this research was aimed for the influence and disturbances for complex and freeform surfaces, this chapter is added to discuss some expected results.

First of all, a curvature of the surface would lead to an increase of reflections, similar to the internal reflections for any lasered groove. Not only this, but the shape of the groove will be affected as well. On first glance, the grooves would become steeper and slightly thinner, because at the edges, there would be more material to remove compared to a flat surface. This combined with the lower intensity of the Gaussian laser beam at the edges could possibly result in this change of groove shape.

The disturbances are expected to have a similar effect as with the flat surface results, mainly because the disturbance effects can be related to the fluence of the laser beam. A higher FOD will result in an even lower fluence, same as with flat surfaces. Because of the curvature of the surface however, a combination of both disturbance influences is expected however. The curve naturally results in a change of incident angle, even if small. It is the same for the FOD. When focusing on one point, the next point will be automatically higher or lower because of the curved surface.

5.5 Modelling results

Next to the data from the experimental dataset, some calculations have been made with the model. These results will be compared to the experimental data.

5.5.1 Influence of the different beam radii

As mentioned, there is a large difference between the different radii of the beam, and the equivalent radius to achieve the same surface for a circular beam spot. These three radii have been put in the model, the resulting groove parameters measured by hand, and compared to the experimental data. This is shown in Figure 39 for 10 layers and varying scanning speed, in focus. Here it can be seen that the experimental values of depth are higher than the model values, with the exception with 500 mm/s scanning speed. One of the possible reasons for the underestimation of groove depth by the modelling, is that the lowering of the ablation threshold due to multiple pulses is not properly taken into account in the models. To confirm this, a similar comparison has been done, but with 20 layers, which is shown in Figure 40. Here the ablation depth of the experiments is again deeper than the model values. At a scanning speed of 2000 mm/s, the difference between the experiment and the model for r_eq is 1.67 µm for 10 layers and 3.07 µm for 20 layers. With the exception for 500 mm/s, the difference seems to always be doubled. From this, it can be concluded that with the current settings, the model does not calculate the depth properly, likely because of an error in the influence of the ablation threshold reduction. Normally the depth reduces per layer, as shown with the experimental results. The fact that, when increasing the number of layers, the experimental depths are even further from the model estimation, confirms this as well.

For the FWHM measurements, in Figure 39, the experimental values are slightly higher than the model results as well. However, when looking at Figure 40, the experiment values lie between the model data. From this, it can then be concluded that the width calculations of the model closely resemble those of the experiments. With a third set at, e.g. 30 layers, it could be determined if the model gives the same FWHM values of the grooves to resemble those of the experiments, to confirm this further. In other words, another comparison between experiments and model can determine if the model gives similar FWHM values as the experiments, since 10 layers was different from the experiments, while 20 layers was similar to the experimental values.

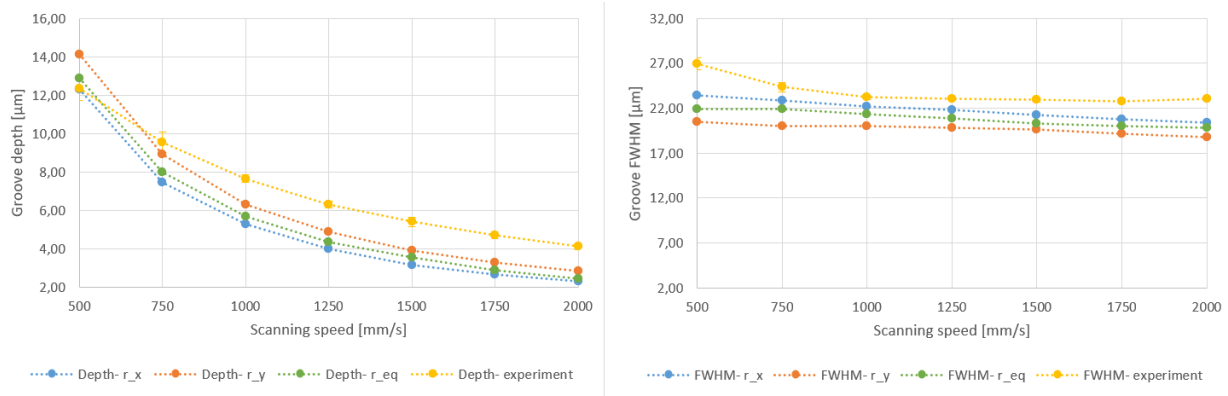

Figure 39: Model results with different radii and the experimental results for the same laser parameters (10 layers, varying scanning speed and in focus).

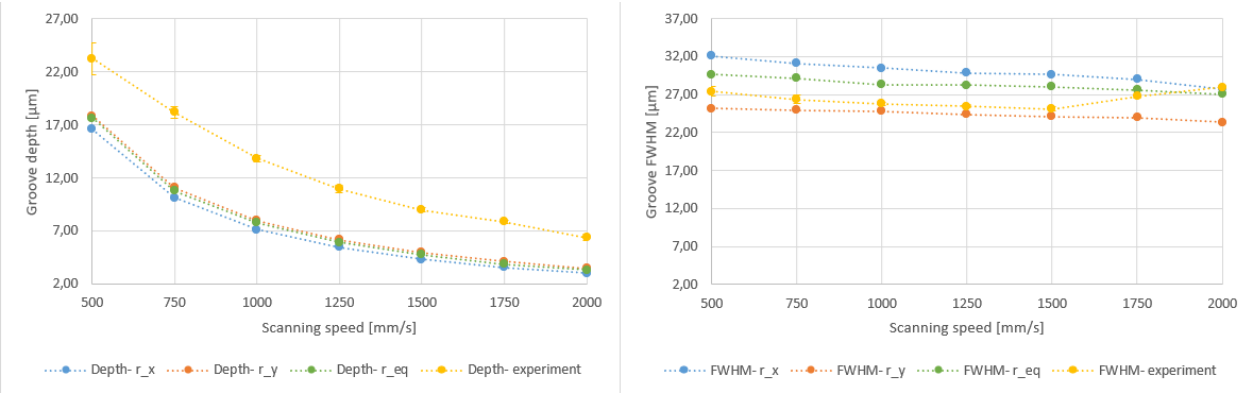

Figure 40: Model results with different radii and experimental results for the same laser parameters (20 layers, varying scanning speed and in focus).

From these figures as well, it can be concluded that the model gives slightly low values when increasing the number or layers when comparing to the experimental data. When looking at Figure 31, when going from 10 to 20 layers, the groove depth almost doubles, for all scanning speeds. But it is the same for the different number of layers as well. For the model however, the depth values increase from around 13 to around 17 µm at a scanning speed of 500 mm/s. For the other speed values too, the increase is only around 1.5 times the depth at 10 layers, instead of the almost times two for the experiments.

The conclusion that the ablation threshold is not properly changed, can be confirmed by Figure 41. In this Figure, the model is used to calculate the depth with increasing FOD. This was done by using the equivalent radius of the laser beam for that FOD value, as described in chapter 5.3. So only the increase in beam spot for larger FOD's was used to check the model ablation depth. It is shown that, when the value for a FOD of 1.5 mm is used, the model gives a flat line as ablation result. In other words, the model calculates that there is no ablation. When looking at Figure 28, where the peak fluence is compared to the FOD, it is shown that the peak fluence for 1.5 mm FOD lies below the ablation threshold of stainless steel (0.32 J/cm²).

The used processing parameters where chosen so that these depth values can be compared to the experimental results shown with the blue curve in Figure 32 and Figure 33. These figures clearly show that there is still ablation of the material, contradicting the model.

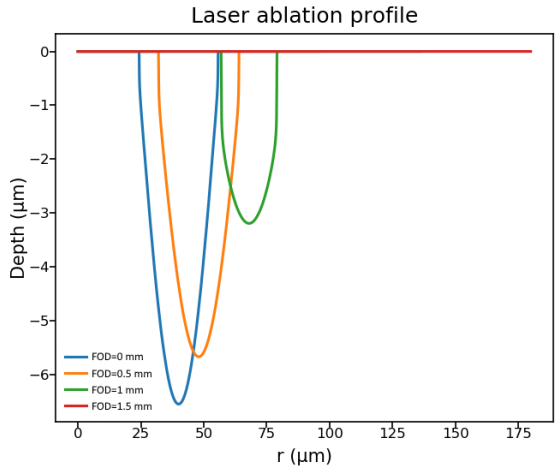

Figure 41: No ablation according to the model for an FOD of 1.5mm or higher.

It should be noted, that to quickly check for an explanation for this model behaviour, some parameters were changed to see if they improved the results. The ablation threshold directly influences the depth of the groove, and as a result did made it possible to "create" ablation with this beam radius of 44.65 μm. Changing the incubation factor however does not have the same effect. When varying this value from 0.05 to 1.8, there was no "new" ablation with this radius. This is why, the implementation of the ablation threshold lowering for multiple pulses seems the primary cause for this deviation. Normally, the incubation factor represents the change in ablation threshold, but this short experiment showed that changing this parameter did not have the described effect. The calculated ablation threshold for multiple pulses in chapter 5.1 also shows this, because this value is much lower than the single pulse threshold.

5.6 Possible model suggestions

Because of limited time, there was no possibility to implement changes to the current model. However, some changes or additions to the model have been thought of and will be discussed in the next paragraphs.

It should also be noted that the model is based on theoretical discussions based on research of femtosecond laser ablation [18]. So, the use when expanding of the model completely depends on the applications for which this is used. If it is used only for preliminary results, for example, to reduce the amount of experiments and replace them with modelling, the suggestions are not needed. Similarly, when a simple comparison is needed between model and experimental results. However, when the model is used as a basis for complex 3D surfaces and CAD applications, the suggestions need to be implemented, because these discuss the main influences on the groove parameters when disturbances are present.

5.6.1 General

To measure the values given by the model, the method of printing and measuring by hand was needed. The option for the model to give these values, instead of only the graphs, for the user would greatly improve the results as well. This would eliminate the possible human errors when measuring or the warping of images when printing. At the same time, this would reduce the time needed for these measurements, and they can be done more easily.

5.6.2 Implementation for elliptical beams

As discussed in previous chapters, the beam of the laser is astigmatic and thus, not circular in shape. To solve this, the model shall implement an option for the beam shape. With this option, the user has the ability to choose the beam spot shape, to either do modelling with real laser beam sizes (elliptical shape), or a more theoretical approach (circular shape).
It could also be implemented that the model gives all 3 results when choosing for an elliptical shape, i.e. that the model calculates the equivalent radius on its own as well. Similarly as done in the previous chapter by hand. This could give as a result, a range for which the actual experimental values will lie in, as was the case for the FWHM in Figure 40.

5.6.3 Implementation of FOD

The implementation to take the FOD into account is another useful addition. The easiest way to properly implement this, is to let the user examine the beam spot at different FOD levels and then to fit a curve through these measurement points so a similar shape as in Figure 5 is achieved. Then to use the curve parameters as input for the model. This way, the model knows the exact progression of the beam when going further from focus.
Another way to implement this, is to give the user the option to give a fluence value as input, instead of calculating this in the model. This way, the user can adjust this parameter more easily, both normally and as a result of a FOD change. As already discussed, the fluence changes according to the FOD, because the beam spot dimensions change.

5.6.4 Implementation of BIA

To implement the effects of a BIA is at quite difficult and extensive, at first glance. This is why only a couple of aspects are discussed here.

The first aspect is the change of beam spot shape. This will no longer be a simple circle or ellipse. As a simple example: when projecting a circle on an angled surface, the projection will become elliptical in shape. In Figure 42, an illustration is shown to clarify this. Here, the rest is the laser beam on the black sample. The projection on the sample is shown below, between the blue lines. The highest intensity of the laser beam is circled with the black line. Here it can be seen that the y radius stays the same, but because of the angle of the sample, the x radius changes, creating an ellipse.
Because the beam has a shape of a cosines hyperbolic in cross section, an angled projection is more difficult to calculate than a projection of a cylinder.

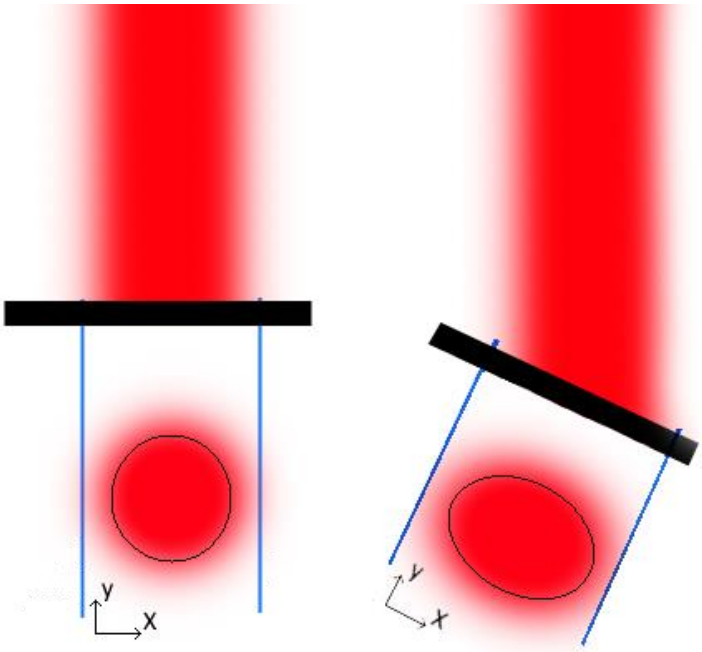

Figure 42: Illustration of how an angled projection changes the spot size.

One of the results of this spot size change is, similarly to the FOD, a change in fluence. This is easily calculated, assuming the same change in dimensions as a circle projected to form an ellipse. Here one of the radii is changed and could then be implemented similarly as discussed for the FOD changes. When assuming a circular initial beam spot, an equivalent radius can be easily calculated as shown below (r_{1-proj}). If there is an elliptical shape, the radii should be kept separate (r_1 and r_2). But this could be combined with the beam spot shape option described in the previous paragraph.

Normally:

$$A_{ellipse} = \pi \cdot r_1 \cdot r_2$$

Because of projection on angled surface:

$$r_1 \rightarrow r_{1-proj} = r_1 \cdot \frac{1}{\cos(BIA)}$$

And so: (13)

$$A_{projected\ ellipse} = \pi \cdot r_1 \cdot r_2 \cdot \frac{1}{\cos(BIA)}$$

If $r_1 = r_2$, then:

$$r_{eq} = r_1 \cdot \sqrt{\frac{1}{\cos(BIA)}}$$

Another aspect regarding BIA, is the different groove form. It should be examined and tested if the change of shape has a large impact on the internal reflection. This should be done for both the experiments and the model. For the experiments, first it should be examined to what extend the internal reflection has an impact on the lasering, and how this is affected by a BIA. Both steps should then be implemented in the model, to achieve more accurate results. Similarly, the incident angle and multiple pulses have an impact on the local surface angle that influence the reflectivity of the surface and the energy absorption [53].

A possible way to implement the BIA is described in [53]. Here a BIA is used to create perpendicular groove walls, created by tilting the sample compared to the laser. Because of this, it was only implemented to include this angle for the shape, no further inclusions of BIA were made.

6 Conclusion and future work

6.1 Conclusion

The influence on groove depth and FWM of the disturbances Focal Offset Distance (FOD) and Beam Incident Angle (BIA) has been examined. This can be used for the partitioning of materials and surfaces, so the processing speed can be optimised, which is an important factor for the industry. For an increase of FOD values, a decrease in groove depth was seen, while the width increased. Some of the processing parameters of number of layers and scanning speed gave similar results for depth and could prove interesting for industrial applications. Namely that a similar depth can be achieved with different processing parameters, and so, the optimal processing speeds can be chosen. The influence of a BIA was found to be very impactful. With the presence of a BIA, the depth seemed to converge to a value depending on the number of layers, while the scanning speed has no influence anymore. For the FWHM, all processing values converged to the same value. Also, some previous conclusions of the processing parameters were contradictory. For example, because of the incident angle, the decreasing depth with increasing scanning speed was no longer the case since the BIA depth was constant for all speeds. Because of these influences, especially for the BIA, it was concluded that using a basic laser for complex surfaces would result in large deviations for the textures.

To complement these results, a model was used to verify these experiments. The current laser ablation model however is still limited with non-inclusion of FOD and incident angle. So only the samples in focus and no incident angle were compared and found that there was a difference in groove dimensions between model and experiments. The trends of the model values were similar to those of the experiments. The magnitude of the model values however was lower than these of the experiments. This could possibly be attributed to the model assumptions and the constants used from the literature. On the other hand, some suggestions, and possibilities to improve and expand the model were given, so the model can later be used for disturbance modelling as well, or be used for the 3D CAD calculations of current research.

6.2 Future work

After this master's thesis project, some additional experiment could be done. These include further examination of the BIA, with smaller angles, to check if there is a more progressive influence. Especially to aid with the possible margins for the 3D CAD calculations, smaller BIA and FOD values should be tested, because of the scale of which these are present for this application. For this application, the values lie closer to 0.1° and 0.05mm for respectively the BIA and FOD. Additionally, the influence of the tilted middle line for the BIA grooves can be further examined, to see if the length of the angled line provides more similar results to the reference sample. Also, tests with properly prepared samples could be done. This can be done as confirmation that the used lasering and measuring method was correct and did avoid large surface roughness influences present on the used samples. Also, additional measurements could be done, to possibly calculate material removal rates, interesting for the industrial applications. Or rearranging data to depict the aspect ratio of the grooves, since it was left out of this research.

The optimization of the model can also be a next step of this research. This would include adding the given suggestions of this research and implementing them in the actual model. Also, further tests should be executed with the model, to examine the correct model parameters. Especially regarding the difference in depth between model and experiments and the stopping of ablation while experiments show grooves are still made with larger FOD values.

When the influence of disturbances is added to the model, this could then be used to aid with current research examining lasering of complex surfaces. At this moment, such a research is being conducted at the Advanced Manufacturing Technology Centre of the University of Birmingham. The model can help expand this research, and possibly be implemented for direct 3D CAD calculations, used in this research for laser polishing Ti implants.

Bibliography

[1] "Advanced Manufacturing Technology Centre - Mechanical Engineering research - University of Birmingham." [Online]. Available: https://www.birmingham.ac.uk/research/activity/mechanical-engineering/advanced-manufacturing/index.aspx. [Accessed: 17-Feb-2020].

[2] "Laser Processing - Advanced Manufacturing Technology Centre - School of Mechanical Engineering - University of Birmingham." [Online]. Available: https://www.birmingham.ac.uk/research/activity/mechanical-engineering/advanced-manufacturing/laser-processing.aspx. [Accessed: 17-Feb-2020].

[3] C. Koepfer, "New Lasers Are Mainstreaming Micro-Machining," *Mod. Mach. Shop*, vol. 76, no. Mod. Mach. Shop, pp. 58–60, 2004.

[4] A. Garcia-Giron, J. M. Romano, A. Batal, A. Michałek, P. Penchev, and S. S. Dimov, "Experimental investigation of processing disturbances in laser surface patterning," *Opt. Lasers Eng.*, vol. 126_artice, no. August, pp. 1–10, 2019.

[5] J. Pina-Estany, A. A. García-Granada, and E. Corull-Massana, "Injection moulding of plastic parts with laser textured surfaces with optical applications," *Opt. Mater. (Amst).*, vol. 79, no. April, pp. 372–380, 2018.

[6] F. Text, "Global $ 6 . 52 Billion Metal Injection Molding (MIM) Market , 2025 : Growing Demand for Small Components in the Automotive , Consumer Products and Medical Equipment Industry - Research and Markets," no. Mim, pp. 1–3, 2017.

[7] W. Yang and J. Zhiwei, "Injection moulding of polymers," in *Advances in Polymer Processing*, Beijng: Beijing University of Chemical Technology, 2009, pp. 175–203.

[8] J. Vera, A. C. Brulez, E. Contraires, M. Larochette, S. Valette, and S. Benayoun, "Influence of the polypropylene structure on the replication of nanostructures by injection molding," *J. Micromechanics Microengineering*, vol. 25, no. 11, pp. 1–10, 2015.

[9] A. K. Singh *et al.*, "Surface micro-structuring of type 304 stainless steel by femtosecond pulsed laser: effect on surface wettability and corrosion resistance," *Appl. Phys. A Mater. Sci. Process.*, vol. 124, no. 12, pp. 1–9, 2018.

[10] A. Grabowski, M. Sozańska, M. Adamiak, M. Kępińska, and T. Florian, "Laser surface texturing of Ti6Al4V alloy, stainless steel and aluminium silicon alloy," *Appl. Surf. Sci.*, vol. 461, no. March, pp. 117–123, 2018.

[11] Y. H. Shin, S. Choi, J. Cho, J. H. Kim, and I. S. Hwang, "Advanced passive design of small modular reactor cooled by heavy liquid metal natural circulation," *Prog. Nucl. Energy*, vol. 83, pp. 433–442, 2015.

[12] J. Diaci, D. Braun, A. Gorki, and J. Moina, "Rapid and flexible laser marking and engraving of tilted and curved surfaces," *Opt. Lasers Eng.*, vol. 49, no. 2, pp. 195–199, 2011.

[13] S. Bruening, K. Du, and A. Gillner, "Ultra-fast micro machining of cylindrical parts with multiple ultra- short pulsed laser sources," *Phys. Procedia*, vol. 83, pp. 167–181, 2016.

[14] S. Vanhemel, "Hierarchical texturing of injection mould materials by femtosecond laser processing [eindwerk]," pp. 1–77, 2019.

[15] M. Ardron, N. Weston, and D. Hand, "A practical technique for the generation of highly uniform LIPSS," *Appl. Surf. Sci.*, vol. 313, pp. 123–131, 2014.

[16] L. Overmeyer, J. F. Duesing, O. Suttmann, and U. Stute, "Laser patterning of thin film sensors on 3-D surfaces," *CIRP Ann. - Manuf. Technol.*, vol. 61, no. 1, pp. 215–218, 2012.

[17] A. Batal, A. Michalek, P. Penchev, A. Kupisiewicz, S. Dimov, and 1, "Laser processing of complex surfaces: polishing and texturing of 3D printed Ti-6Al-4V spherical shells," Edgbaston, Birmingham, 2020.

[18] N. N. Nedialkov, S. E. Imamova, and P. A. Atanasov, "Ablation of metals by ultrashort laser pulses," *J. Phys. D. Appl. Phys.*, vol. 37, no. 4, pp. 638–643, 2004.

[19] F. Di Niso, C. Gaudiuso, T. Sibillano, F. P. Mezzapesa, A. Ancona, and P. M. Lugarà, "Role of heat accumulation on the incubation effect in multi-shot laser ablation of stainless steel at high repetition rates," *Opt. Express*, vol. 22, no. 10, p. 12200, 2014.

[20] N. Ackerl and K. Wegener, “Ablation characteristics of alumina and zirconia ceramics on ultra-short pulsed laser machining,” *J. Laser Micro Nanoeng.*, vol. 14, no. 2, pp. 168–172, 2019.
[21] P. S. Dimov, “Fundamentals of Laser-Based Materials Processing MSc Laser-Based Manufacturing,” *Laser based Manuf. - Cl.*, pp. 1–42, 2020.
[22] B. J. Li, M. Zhou, W. Zhang, G. Amoako, and C. Y. Gao, “Comparison of structures and hydrophobicity of femtosecond and nanosecond laser-etched surfaces on silicon,” *Appl. Surf. Sci.*, vol. 263, pp. 45–49, 2012.
[23] B. Vermang and E. Wieërs, “Golfbeweging,” in *Fysica voor industrieel ingenieurs deel1 [cursus]*, Diepenbeek: Gezamelijke opleiding industriële ingenieurswetenschappen Uhasselt & KU Leuven, 2016, p. 155.
[24] “Femtosecond Lasers - Thorlabs.” [Online]. Available: https://www.thorlabs.com/navigation.cfm?guide_id=2024. [Accessed: 10-Mar-2020].
[25] A. Batal *et al.*, “Effects of laser processing conditions on wettability and proliferation of Saos-2 cells on CoCrMo alloy surfaces,” *Advanced Optical Technologies*, pp. 1–12, 2019.
[26] F. Dupont, S. Stoukatch, P. Laurent, S. Dricot, and M. Kraft, “355 nm UV laser patterning and post-processing of FR4 PCB for fine pitch components integration,” *Opt. Lasers Eng.*, vol. 100, no. July 2017, pp. 186–194, 2018.
[27] “Light: Electromagnetic waves, the electromagnetic spectrum and photons (article) | Khan Academy.” [Online]. Available: https://www.khanacademy.org/science/physics/light-waves/introduction-to-light-waves/a/light-and-the-electromagnetic-spectrum. [Accessed: 10-Mar-2020].
[28] R. Paschotta, “M2 Factor.” [Online]. Available: https://www.rp-photonics.com/m2_factor.html. [Accessed: 10-Mar-2020].
[29] “Gaussian beam.” [Online]. Available: https://en.wikipedia.org/wiki/Gaussian_beam. [Accessed: 10-Mar-2020].
[30] S. Xiao, B. Schöps, and A. Ostendorf, “Selective Ablation of Thin Films by Ultrashort Laser Pulses,” *Phys. Procedia*, vol. 39, pp. 594–602, 2012.
[31] K. M. Tanvir Ahmmed, C. Grambow, and A. M. Kietzig, “Fabrication of micro/nano structures on metals by femtosecond laser micromachining,” *Micromachines*, vol. 5, no. 4, pp. 1219–1253, 2014.
[32] “Focus Variation Technology | Alicona.” [Online]. Available: https://www.alicona.com/en/focus-variation/. [Accessed: 10-Mar-2020].
[33] “Facilities and equipment - Advanced Manufacturing Technology Centre - Mechanical Engineering - University of Birmingham.” [Online]. Available: https://www.birmingham.ac.uk/facilities/advanced-manufacturing/index.aspx. [Accessed: 10-Mar-2020].
[34] R. Leach, “Surface topography measurement instrumentation,” in *Fundamental Principles of Engineering Nanometrology*, Second edi., Oxford: Elsevier Inc., 2014, pp. 133–204.
[35] “Young’s equation.” [Online]. Available: https://www.kruss-scientific.com/services/education-theory/glossary/youngs-equation/. [Accessed: 12-Mar-2020].
[36] E. L. Decker, B. Frank, Y. Suo, and S. Garoff, “Physics of contact angle measurement .Pdf,” vol. 156, pp. 177–189, 1999.
[37] “ramé-hart Contact Angle.” [Online]. Available: http://www.ramehart.com/contactangle.htm. [Accessed: 12-Mar-2020].
[38] S. Zarghami, T. Mohammadi, M. Sadrzadeh, and B. Van der Bruggen, “Superhydrophilic and underwater superoleophobic membranes - A review of synthesis methods,” *Prog. Polym. Sci.*, vol. 98, pp. 101–166, 2019.
[39] C. Schlaich, Q. Wei, and R. Haag, “Mussel-Inspired Polyglycerol Coatings with Controlled Wettability: From Superhydrophilic to Superhydrophobic Surface Coatings,” *Langmuir*, vol. 33, no. 38, pp. 9508–9520, 2017.
[40] E. Bormashenko, “Why does the Cassie-Baxter equation apply?,” *Colloids Surfaces A Physicochem. Eng. Asp.*, pp. 1–4, 2008.
[41] H. Ogihara, J. Xie, and T. Saji, “Factors determining wettability of superhydrophobic paper prepared by spraying nanoparticle suspensions,” *Colloids Surfaces A Physicochem. Eng. Asp.*, vol. 434, pp.

35–41, 2013.
[42] "ramé-hart Contact Angle." [Online]. Available: http://www.ramehart.com/contactangle.htm. [Accessed: 13-Mar-2020].
[43] P. Gamonal-Repiso, M. Sánchez-Soto, S. Santos-Pinto, and M. L. Maspoch, "Improvement of the replication quality of randomly micro-textured injection-moulding components using a multi-scale surface analysis," *J. Manuf. Process.*, vol. 42, no. April, pp. 67–81, 2019.
[44] C. Rytka, J. Lungershausen, P. M. Kristiansen, and A. Neyer, "3D filling simulation of micro- and nanostructures in comparison to iso- and variothermal injection moulding trials," *J. Micromechanics Microengineering*, vol. 26, no. 6, 2016.
[45] N. Zhang, H. Zhang, C. Stallard, F. Fang, and M. D. Gilchrist, "Replication integrity of micro features using variotherm and vacuum assisted microinjection moulding," *CIRP J. Manuf. Sci. Technol.*, vol. 23, pp. 20–38, 2018.
[46] C. K. Huang, "Polymeric nanofeatures of 100 nm using injection moulding for replication," *J. Micromechanics Microengineering*, vol. 17, no. 8, pp. 1518–1526, 2007.
[47] Y. Zhang, H. N. Hansen, and S. Sørensen, "Replication of micro-pillars by PEEK injection moulding with CrN-coated Ni tool," *Int. J. Adv. Manuf. Technol.*, vol. 80, no. 1–4, pp. 383–388, 2015.
[48] P. Parenti, D. Masato, M. Sorgato, G. Lucchetta, and M. Annoni, "Surface footprint in molds micromilling and effect on part demoldability in micro injection molding," *J. Manuf. Process.*, vol. 29, pp. 160–174, 2017.
[49] Y. K. Shen, "Comparison of height replication properties of micro-injection moulding and micro-injection-compression moulding for production of microstructures on lightguiding plates," *Plast. Rubber Compos.*, vol. 36, no. 2, pp. 77–84, 2007.
[50] C. Hopmann *et al.*, "Injection moulding of optical functional micro structures using laser structured, PVD-coated mould inserts," *AIP Conf. Proc.*, vol. 1664, no. May, p. 110003, 2015.
[51] Y. Zhang, D. B. Pedersen, A. S. Gøtje, M. Mischkot, and G. Tosello, "A Soft Tooling process chain employing Additive Manufacturing for injection molding of a 3D component with micro pillars," *J. Manuf. Process.*, vol. 27, pp. 138–144, 2017.
[52] O. N. T. H. E. Cover, "Advanced materials & processes," vol. 12, no. 1, pp. 17–20, 2014.
[53] D. Bruneel *et al.*, "Model for ultrafast laser micromachining," vol. 1052010, no. February, p. 38, 2018.
[54] "RP Photonics Encyclopedia - beam expanders, telescopes, zoom, variable magnification." [Online]. Available: https://www.rp-photonics.com/beam_expanders.html. [Accessed: 06-May-2020].
[55] "Advantages of Using Beam Expanders | Edmund Optics." [Online]. Available: https://www.edmundoptics.co.uk/knowledge-center/application-notes/lasers/advantages-of-using-beam-expanders/. [Accessed: 06-May-2020].
[56] J. M. Romano, A. Garcia-Giron, P. Penchev, and S. Dimov, "Triangular laser-induced submicron textures for functionalising stainless steel surfaces," *Appl. Surf. Sci.*, vol. 440, pp. 162–169, 2018.
[57] "Beam'R2 - XY Scanning Slit Beam Profiler | DataRay Inc." [Online]. Available: https://www.dataray.com/collections/scanning-slit-beam-profilers/products/beamr2-xy-scanning-slit-beam-profiler-system. [Accessed: 22-May-2020].
[58] J. M. Romano, M. Gulcur, A. Garcia-Giron, E. Martinez-Solanas, B. R. Whiteside, and S. S. Dimov, "Mechanical durability of hydrophobic surfaces fabricated by injection moulding of laser-induced textures," *Appl. Surf. Sci.*, vol. 476, no. November, pp. 850–860, 2019.
[59] R. Gomeringer *et al.*, "Oberflächen," in *Tabellenbuch metal*, Haan-Gruiten: verslag Europa-Lehrmittel, 2017, p. 102.
[60] W. Dax *et al.*, "Ruwheid," in *TABELLENBOEK voor METAALTECHNIEK*, Mechelen: Plantyn, 2011, p. 94.
[61] E. Audouard and E. Mottay, "Engineering model for ultrafast laser microprocessing," *Front. Ultrafast Opt. Biomed. Sci. Ind. Appl. XVI*, vol. 9740, no. March 2016, p. 974016, 2016.
[62] E. Audouard, J. Lopez, B. Ancelot, K. Gaudfrin, R. Kling, and E. Mottay, "Optimization of surface engraving quality with ultrafast lasers," *J. Laser Appl.*, vol. 29, no. 2, p. 022210, 2017.
[63] W. Liu, M. Sun, Y. Guo, Z. Jiao, R. Wu, and X. Pan, "Ablation characteristics of aluminum alloy and stainless steel induced by picosecond laser pulses," in *Pacific Rim Laser Damage 2019: Optical*

Materials for High-Power Lasers, 2019, vol. 11063, p. 44.
[64] B. Nagarajan, “Parameters for ablation model [email].” 2020.
[65] “RP Photonics Encyclopedia - astigmatism, aberrations, human eye, laser beams, focus position, dioptric power.” [Online]. Available: https://www.rp-photonics.com/astigmatism.html. [Accessed: 24-May-2020].